ANALYSIS OF IMAGE FORMATION WITH THINNED RANDOM ARRAYS

D.Y. Tseng and B.H. Soffer

Hughes Research Laboratories
3011 Malibu Canyon Road
Malibu, CA 90265

June 1979

F49620-77-C-0052

Annual Report
15 February 1978 through 15 February 1979

Sponsored by
AIR FORCE OFFICE OF SCIENTIFIC RESEARCH
Building 410
Bolling Air Force Base, Washington, DC 20332

UNCLASSIFIED

SECURITY CLASSIFICATION OF THIS PAGE (When Data Entered)

REPORT DOCUMENTATION PAGE	READ INSTRUCTIONS BEFORE COMPLETING FORM
1. REPORT NUMBER: AFOSR-TR-79-0894	2. GOVT ACCESSION NO. / 3. RECIPIENT'S CATALOG NUMBER
4. TITLE (and Subtitle): ANALYSIS OF IMAGE FORMATION WITH THINNED RANDOM ARRAYS	5. TYPE OF REPORT & PERIOD COVERED: Annual Report 15 Feb 1978-15 Feb 1979 / 6. PERFORMING ORG. REPORT NUMBER
7. AUTHOR(s): David Y. Tseng and Bernard H. Soffer	8. CONTRACT OR GRANT NUMBER(s): F49620-77-C-0052
9. PERFORMING ORGANIZATION NAME AND ADDRESS: Hughes Research Laboratories, 3011 Malibu Canyon Road, Malibu, CA 93065	10. PROGRAM ELEMENT, PROJECT, TASK AREA & WORK UNIT NUMBERS: 61102F, 2305/B1
11. CONTROLLING OFFICE NAME AND ADDRESS: Air Force Office of Scientific Research, Building 410, Bolling AFB, DC 20332	12. REPORT DATE: June 1979 / 13. NUMBER OF PAGES: 85
14. MONITORING AGENCY NAME & ADDRESS (if different from Controlling Office)	15. SECURITY CLASS. (of this report): UNCLASSIFIED / 15a. DECLASSIFICATION DOWNGRADING SCHEDULE
16. DISTRIBUTION STATEMENT (of this Report): 2305 B1	
17. DISTRIBUTION STATEMENT (of the abstract entered in Block 20, if different from Report): 77 p.	
18. SUPPLEMENTARY NOTES	
19. KEY WORDS (Continue on reverse side if necessary and identify by block number): Imaging, Antennas, Thinned Arrays	

20. ABSTRACT (Continue on reverse side if necessary and identify by block number)

Very high resolution imaging systems, regardless of wavelength, require large apertures with a high resolution, low sidelobe level and high gain. These apertures are often considered to be technically and economically infeasible. We investigated the efficacy of using very sparse arrays of randomly placed small antenna elements in imaging systems. The properties of these arrays are established in antenna theory. What we have done is to make the first demonstration of their

DD FORM 1 JAN 73 1473 EDITION OF 1 NOV 65 IS OBSOLETE

UNCLASSIFIED

SECURITY CLASSIFICATION OF THIS PAGE (When Data Entered)

172 600

application in imaging systems. Computer simulation studies were made for coherent, partially coherent, and incoherent imaging. These were done using various conditions, including variable signal-to-noise ratio and phase aberration, but with monochromatic illumination. We showed that, for incoherent imaging, a large degree of thinning down to 6% of the number of full array elements (4096) produces image quality comparable to that produced by the full array. For broad-band polychromatic incoherent imaging, even larger degrees of thinning, down to 3%, were similarly effective. The fractional degree of thinning allowable for incoherent imaging in principle is inversely proportional to the square root of the number of elements in the full array, which number is equivalent to the number of elements resolved in the full array. The arrays, which are easy to design, degrade gracefully when large fractions of the elements are removed. For coherent imaging applications, random arrays do not offer significant advantages over full arrays.

TABLE OF CONTENTS

LSIT OF ILLUSTRATIONS

SECTION 1

INTRODUCTION AND SUMMARY

Recent requirements for very high resolution imaging systems have produced a great demand for apertures with high resolution, low sidelobe levels, and high gain. To achieve the resolutions desired, extremely large apertures are needed. The realization of such apertures is generally considered to be either economically or technically infeasible. Table 1 gives some representative numbers for such arrays. The numbers are astronomically large in many cases. Hence, attention has been focused on large arrays. Arrays with uniformly spaced elements produce undesirable grating lobes. For these arrays, there exists a maximum spacing between elements if the grating lobes are to be removed from the object. The number of elements required in such uniform arrays would be very large and in direct proportion to the aperture dimension. Therefore, the investigation of arrays with a reduced number of elements (the "thinned arrays"), which possess the desired characteristics of the full arrays, has been of recent interest.

Arrays with incommensurable element spacings usually have aperiodic radiation pattern functions. Consequently, the number of elements required is not directly determined by the aperture dimension. However, there is no general theory available for the algorithmic design of this class of arrays. Many of the designs to date have been based on trial-and-error methods using high-speed computers. But there is never any assurance that any particular trial will produce a successful design.

One class of arrays exists that possesses the desired characteristics of high-resolution imaging systems and yet requires surprisingly few elements to achieve these features. This class, random arrays, is well established in antenna theory and has been generally applied to signal-detection applications. The properties of such arrays are approached from a probabilistic point of view, even though the performance of any particular array itself is not probabilistic. That is, once the positions of the array elements are determined, the properties of the random array are completely deterministic. A prime advantage

Table 1. Representative Full Array Requirements

Wavelength, μm	Resolution, cm	Range, km	Aperture Dimension, m	Array Element Size, m	Number of Elements Required
10	10	10,000	1,000	2	2.5×10^5
10	20	40,000	2,000	2	1.0×10^6
3.5	10	10,000	350	1	1.2×10^5
0.5	10	10,000	50	1	2.5×10^3
0.5	10	1,000	5	1	25

6249

of these arrays is that predictions on the array's performance can be made before carrying out detailed computations. Therefore, designing the array is reduced to playing a game in which the probability of success is determined to be sufficiently large before any actual evaluation of the final array design is attempted. Other advantages of random arrays are discussed below.

For random arrays, the sidelobe level is closely related to the number of elements and, to a much lesser degree, to the total aperture dimension. The resolution, or main beam width, depends on the total aperture dimension; the directive gain is proportional to the number of elements used if the average spacing is large. Consequently, extremely high resolution can be achieved with very few elements. On the other hand, for a given number of elements, higher resolution can be obtained by spreading these elements over a large aperture, with the sidelobe levels remaining substantually the same and the directive gain constant.

We have applied the concept of random arrays to imaging systems to determine their capabilities and limitations for imaging applications. To the best of our knowledge, this is the first demonstration of the utilization of thinned random arrays in imaging systems. Computer simulation studies have been carried out here for incoherent, partially coherent, and coherent imaging. These investigations were performed using various conditions, including variable signal-to-noise ratio (S/N) and phase aberration in the imaging system, with monochromatic and polychromatic illumination of the object. However, no attempt was made to post-process the reconstructed images for any type of enhancement.

The results show that good quality images can be obtained for random arrays with very few elements, even down to only 6% of the number of elements of a uniform full array of 4096 elements. (The number of elements in the full array is equivalent to the number of elements resolved by the full array in its field of view (FOV)). These results hold for a low (e.g., > 3) S/N and a high-intensity background in the image. For broadband polychromatic incoherent imaging, the number of elements can be even further reduced. In addition, this

image quality can be achieved by many distinct random-array configurations. The image resolution can be maintained as the number of array elements is reduced if the aperture dimension is fixed for each random thinned array. The quality of the image degrades, as shown by the appearance of higher (random) background levels as the number of array elements is reduced. This is a manifestation of the increased sidelobe level of the random array as the number of elements is reduced. For a given number of elements, the simulation results exhibited an improvement in image resolution as the number of elements was spread over larger aperture dimensions. The overall background levels in these images remained essentially constant. These encouraging results, which were obtained without utilizing any averaging or interpolation post-processing techniques in the aperture plane for image enhancement, lead us to believe that similarly impressive performance can be achieved in practice.

We have studied the effects of background, S/N, and phase aberrations (such as those caused by turbulence and any figure disposition in the case of incoherent imaging). For coherent imaging, the effects of speckle were examined, and a method of speckle elimination was studied. The determination of the dependence of the maximum thinning factor possible to retain good quality in the image was investigated as a function of the pertinent parameters, including the total number of elements and S/N.

To present a comprehensive exposition of our results, we have incorporated in this report the principle results of the previous reporting periods along with the two studies performed in this period. In this year, a study was made of the use of broadband polychromatic radiation incoherent imaging. Partially coherent imaging was modeled as well, and computer simulations were performed.

SECTION 2

TECHNICAL DISCUSSION

A. IMAGING CONCEPTS

The imaging process may be viewed in two complementary ways. Although mathematically equivalent and related by theorems of Fourier transformation, one view or the other reveals special insights and simplifications, depending on the particular circumstances. We may, for example, view the imaging process as a convolution of the object field and the radiation or antenna pattern of the aperture, as is the case for coherent imaging. If the aperture is a large lens or collecting mirror, then its radiation or diffraction pattern, which is the Fourier transform of the aperture configuration, will be a sharply peaked function in angular extent with only small subsidiary sidelobes. Convolving this pattern with the object field produces an image field the quality of which depends on the strength and degree of sharpness of the mainlobe and the weakness and disposition of the sidelobes.

Alternatively, we may view the imaging process by considering the Fourier transformation of the object into its spectrum of spatial frequencies. If only the intensities of the image and object are of interest, then the Fourier transformation of the intensity representation of the object will appear in the far field at the aperture, or entrance pupil, of the imaging instrument as the (complex) visibility pattern; it is sometimes called the partial coherence transform vis-à-vis the Van Citert-Zernike theorem.* This coherence transform is sampled to some degree in the aperture plane, depending on the nature and size of the collecting aperture. The amplitude of the transform is the classical visibility of fringes as a function of spatial frequency given by the separation of the aperture elements. The phase of the transform is the spatial phase of these fringes referred to the optical axis or focus of the system. This sampled function is then inversely

*This theorem is the spatial analog of the Wiener-Khintchine theorem relating the power spectrum and temporal correlation for stationary processes.

transformed to form the image. The quality of the image, from this point of view, depends on the degree to which the irradiance of the object has been sampled in the aperture plane and the disposition of the sampling elements. Insufficient and regular sampling of the aperture will produce an image not only lacking in all the correct details at the missing (i.e., unsampled) spatial frequencies, but will also produce vivid spurious image information caused by large uncompensated Fourier terms.

To amplify the description of imaging and to cast these concepts in more concrete terms, it is instructive to put the results in more formal mathematical terms. The mathematical representations of the imaging process take especially simple form in the limiting cases of completely coherent and completely incoherent imaging. These cases are of practical interest as well, for they are good approximations to conditions encountered most often. However, we did not limit our study to these cases.

1. Coherent Imaging

Coherent imaging systems are linear in complex field amplitude. From diffraction considerations, the field distributions of the image, $U_i(x,y)$, and object, $U_o(u,v)$, are related by the convolution integral

$$U_i(x,y) = \iint_{obj} h(x-u,\ y-v)\ U_o(u,v)\ dudv \quad , \tag{1}$$

where $h(x-u, y-v)$ is the impulse response of the imaging system. A generalized schematic of an imaging system is shown in Figure 1. The pupil function $P(x',y')$ has the property that

$$P(x',y') = \begin{cases} 1 \text{ within the aperture configuration} \\ \\ 0 \text{ elsewhere.} \end{cases} \tag{2}$$

This function accounts for the finite extent of the pupil, or aperture, of the imaging system. The system impulse function is directly related

to the pupil function by a Fourier transformation:

$$h(x,y) = \iint_{aper} P(\alpha,\beta) e^{-j2\pi(x\alpha+y\beta)} \, d\alpha d\beta \, . \qquad (3)$$

Thus, for a given wavelength, the imaging properties of a system are completely determined by the pupil function, or aperture, of the imaging system.

Two quadratic phase terms that normally appear in Eq. 3 have been neglected in the diffraction formulation of the imaging system. These terms convey phase curvature information and can be dropped directly if imaging is considered to be between two spherical surfaces. For plane surfaces, these terms can also be neglected. The justification is based on the fact that the resultant image is usually sensed with detectors that respond to intensities. One of these quadratic phase terms only modifies the phase distribution of light and cannot affect the resultant detected image intensities. The second quadratic phase term can be neglected also if the imaging system maps neighboring points in the object plane onto neighboring points in the image plane. This condition is satisfied for most cases where the object is of small angular extent. Mathematical details of these concepts can be found in J.W. Goodman, Introduction to Fourier Optics.

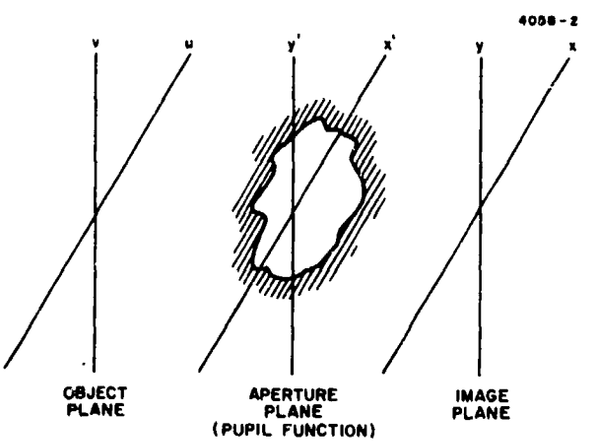

Figure 1. Schematic of generalized imaging system.

The convolution integral, Eq. 1, can be conveniently recast into its spatial frequency spectrum representation by Fourier transformation. Denoting the Fourier transforms of U and h by $\tilde{U}$ and $\tilde{h}$, respectively, the Fourier representation of Eq. 1 is

$$\tilde{U}_i(f_x,f_y) = \tilde{h}(f_x,f_y)\, \tilde{U}_o(f_x,f_y) \quad , \tag{4}$$

where f_x and f_y are the Fourier spatial frequency components. Here, $\tilde{h}(f_x,f_y)$ is known as the coherent transfer function (CTF). Recalling from Eq. 3 that h(x,y) is already the Fourier transform of the pupil function P(x,y), then

$$\tilde{h}(f_x,f_y) = P(f_x,f_y) \quad , \tag{5}$$

and Eq. 4 becomes

$$\tilde{U}_i(f_x,f_y) = P(f_x,f_y)\, \tilde{U}_o(f_x,f_y) \quad , \tag{6}$$

where magnification and image inversion have been ignored. The relationship between the coherent transfer function $\tilde{h}$ and the pupil function (or aperture) P is a direct and simple one. In the Fourier transform representation, therefore, the pupil function (or aperture) samples the Fourier spatial frequency components of the object transform field. The image can be reconstructed from the sampled frequency components by an inverse transformation of $\tilde{U}_i(f_x,f_y)$.

As Eq. 6 shows, diffraction effects of the imaging system are manifested by the finite extent of the pupil function. That is, high spatial frequency components of the object transform field are "cut off" or not sampled. From another point of view, the high-frequency components of the object field diffract to a greater angular extent than the low-frequency components: they are not "intercepted" by the finite aperture of the imaging system. To reconstruct only the high-frequency content of the object (e.g., the edge content), it would be

necessary to sample only the high spatial frequency components of the object transform field. In this case, an annular aperture would be adequate.

2. Incoherent Imaging

Incoherent imaging systems can be viewed from the same approach as described above. For such incoherently illuminated objects, the imaging system is linear in intensity distribution. From diffraction considerations, and representing the image and object field intensities by $I_i(x,y)$ and $I_o(u,v)$, respectively, these field intensities are related by the convolution integral

$$I_i(x,y) = \iint_{obj} |h(x-u,\ y-v)|^2\ I_o(u,v)\ dudv\ , \qquad (7)$$

where $h(x-u,\ y-v)$ is again the impulse response of the imaging system. By forming the intensity of Eq. 1 and imposing the condition of statistical independence (incoherence) on the phasor amplitudes across the object, Eq. 7 can be derived from Eq. 1. In general, the statistical nature (or coherence) of the object phasor amplitude determines the form of the imaging equations.

The image field intensity is also determined by the system impulse response $h(x,y)$, which, in turn, is related to the pupil function $P(x',y')$ by Eq. 3. However, the mapping in this case is carried out by $|h(\alpha,\beta)|^2$, the magnitude squared of the system impulse function. The function $|h|^2$, known as the point spread function (PSF), gives, for finite apertures, the degradation of a δ-function (point) source through the imaging system.

Because of the convolution form of Eq. 7, it can be recast into its spatial frequency spectrum representation also. Denoting the Fourier transforms of I and $|h|^2$ by $\tilde{I}$ and $\tilde{H}$, respectively, the Fourier representation of Eq. 7 is

$$\tilde{I}_i(f_x,f_y) = \tilde{H}(f_x,f_y)\ \tilde{I}_o(f_x,f_y)\ . \qquad (8)$$

The function $\tilde{H}(f_x,f_y)$ is commonly called the optical transfer function (OTF) of the incoherent imaging system, and its modulus $|\tilde{H}(f_x,f_y)|$ is known as the modulation transfer function (MTF). In the Fourier transform representation, the OTF acts as a complex weighting factor in mapping the Fourier spatial frequency components of the object field intensity into image Fourier spatial frequency components. The image can thus be reconstructed from the mapped frequency components in transform space by an inverse transformation of $\tilde{I}_i(f_x,f_y)$

Both the CTF, $h(f_x,f_y)$, and OTF, $\tilde{H}(f_x,f_y)$, involve the system impulse response $h(\alpha,\beta)$. There exists a specific relationship between them. The autocorrelation theorem can be used to show that

$$\tilde{H}(f_x,f_y) = \iint_{\text{aper}} \tilde{h}(\alpha,\beta)\ \tilde{h}^*(\alpha+f_x,\ \beta+f_y)\ d\alpha d\beta \qquad (9)$$

and thus that the OTF is the autocorrelation of the CTF. Using Eq. 5, the above relationship can be reduced further to show that the OTF $\tilde{H}(f_x,f_y)$ is the autocorrelation of the pupil function (or aperture) $P(x',y')$:

$$\tilde{H}(f_x,f_y) = \iint_{\text{aper}} P(\alpha,\beta)\ P^*(\alpha+f_x,\ \beta+f_y)\ d\alpha d\beta \ . \qquad (10)$$

There is an interesting and important geometric interpretation to the autocorrelation function of the aperture distribution. It counts or measures the distribution of all element pairs, discrete or differential, as a function of pair separations, independent of the absolute position of the elements. This may be readily seen by considering a one-dimensional array of discrete elements irregularly disposed on a regular lattice. The first point (zero separation) of the autocorrelation function is the result of multiplying the array with itself, and merely counts the number of elements in the array. Displacing the array over itself by one unit produces overlaps wherever there were unit separations in the array itself; on multiplication, the number of

pairs of unit separation is counted. Similarly, the larger displacements measure the existence of larger separation pairs. Since the separation of a pair exists in spatial frequency space, the OTF for incoherent light can be viewed as a weighting function with a modulus equal to the number of pairs of elements at each spatial frequency.

3. Partially Coherent Imaging Transfer Function

The concept of a linear system impulse response can still be used, even in the case of partially coherent imaging, although its representation is somewhat more complex. Recalling the definition of the mutual coherence function $\Gamma(\bar{x}_1,\bar{x}_2,t_1t_2)$ as the cross correlation of the fields at $U(\bar{x}_1,t_1)$ and $U(\bar{x}_2,t_2)$, and assuming the fields are stationary in time, Γ may be written as a function of difference in time $\tau = t_1 - t_2$:

$$\Gamma(\bar{x}_1,\bar{x}_2,\tau) = \langle U(\bar{x}_1,\ t+\tau)\ U^*(\bar{x}_2,t)\rangle \quad , \tag{11}$$

where the bar notation $(\bar{x}_i)$ indicates a two-dimensional spatial vector (x_i,y_i). The coherence function satisfies the wave equation and therefore propagates, as does light itself, with the effects of diffration. As a result, the Fourier components of the coherence function for each carrier frequency at the image may be related to that at the object by an impulse response function not unlike that for fields themselves:

$$\tilde{\Gamma}(\bar{x}_1,\bar{x}_2,\omega) = \iiiint_{\text{object}} h\,(\bar{x}_1-\bar{u}_1,\ \omega)\ \ h^*\,(\bar{x}_2-\bar{u}_2,\ \omega)\ \ \tilde{\Gamma}(\bar{u}_1,\bar{u}_2,\omega)\ d\bar{u}_1 d\bar{u}_2 \ , \tag{12}$$

where $\tilde{\Gamma}(\omega)$ is the Fourier transform of $\Gamma(\tau)$.

Assuming the quasi-monochromatic approximation

$$\tilde{\Gamma}(\bar{u}_1,\bar{u}_2,\omega) = \tilde{\Gamma}(\bar{u}_1\bar{u}_2,0)\ \delta(\omega - \omega) \quad , \tag{13}$$

we may write, after retransformation and simplification of the integral,

$$\Gamma(\bar{x}_1,\bar{x}_2,\tau) = e^{i\bar{\omega}\tau} \iiiint_{\text{object}} h(\bar{x}_1-\bar{u}_1,\ \omega)\ \ h^*(\bar{x}_2-\bar{u}_2,\ \omega)\ \Gamma(\bar{u}_1,\bar{u}_2,0)d\bar{u}_1d\bar{u}_2 \ , (14)$$

where $\bar{\omega}$ is the mean carrier frequency. This relates the mutual coherence of the object and image. Since the intensity in the image equals $\Gamma(\bar{x}_1,\bar{x}_1,0)$ of the image, we may write

$$I(x_1) = \iiiint_{\text{object}} [h(\bar{x}_1-\bar{u}_1,\ \omega)\ \ h^*(\bar{x}_2-\bar{u}_2,\ \omega)]\ \ \Gamma(\bar{u}_1,\bar{u}_2,0)\ d\bar{u}_1d\bar{u}_2 \ , \ (15)$$

where the bracketed quantity may be considered to be the impulse response. For numerical or experimental analysis, the image intensity can be generated from Eq. 15. Equivalently, for a given form of Γ in terms of the field or intensity, Eq. 15 can be written entirely as a linear superposition of object mutual intensities. $\Gamma(\bar{u}_1,\bar{u}_2,0)$ is sometimes called the mutual intensity $J(\bar{u}_1,\bar{u}_2)$.

Particular explicit models of the coherence $\Gamma(\bar{u}_1,\bar{u}_2)$ of the object fields allow particular development of the image intensity $I(\bar{x}_1)$ in terms of the object fields or intensities. Of course, Fourier transforming the impulse response relation (Eq. 15) by the convolution theorem recasts it into the form of a linear transfer function. Four-dimensional convolution or Fourier transforms on sizable images will exceed the capabilities of most computers.

To simplify our computer calculations, we consider an optical system with transmission function for mutual intensity $K(\bar{u}_1,\bar{x}_1)$. Using scale-normalized coordinates where the object point and its Gaussian image have the same coordinate numbers, the transmission of the mutual intensity is given by:

$$J_I(\bar{x}_1,\bar{x}_2) = \iiiint_{\text{object}} J_o(\bar{u}_1,\bar{u}_2)\ K(\bar{u}_1,\bar{x}_1)\ K^*(\bar{u}_2,\bar{x}_2)\ d\bar{u}_1d\bar{u}_2 \ . \qquad (16)$$

A second major assumption we will make, besides monochromaticity, is that the object is small enough to form an isoplanatic region. In this case, the transmission function K is a function only of the differences in coordinates, for example, $K(\bar{x} - \bar{u})$, and not of the coordinates themselves. Then Eq. 16 becomes

$$J_I(\bar{x}_1,\bar{x}_2) = \iiiint_{\text{object}} J_o(\bar{u}_1,\bar{u}_2)\, K(\bar{x}_1-\bar{u}_1)\, K^*(\bar{x}_2-\bar{u}_2)\, d\bar{u}_1 d\bar{u}_2 \quad . \qquad (17)$$

This relationship is a convolution and we can apply the convolution theorem to the Fourier transforms of the parameters to obtain

$$\tilde{J}(f,g;f',g') = \tilde{J}(f,g;f',g')\, \tilde{K}(f,g)\, \tilde{K}^*(-f',-g') \quad . \qquad (18)$$

The transmission of mutual intensity is seen to still be a four-dimensional linear system. Note also that the Fourier transforms are four dimensional.

The above formulation is simple in form, but still leads to significant problems in terms of implementation in digital image processing. For example, in our simulations the smallest basic image is represented by an array of 128 x 128 pixels. To represent the mutual intensity for this image would require 2^{28} complex numbers, which is far in excess of available storage. Also, computing the four-dimensional Fourier transforms for such an image is computationally prohibitive, even using fast Fourier transform techniques.

To mitigate the data storage problem, we use the degree of coherence, μ, defined by

$$\mu(\bar{u}_1,\bar{u}_2) = \frac{J(\bar{u}_1,\bar{u}_2)}{\sqrt{I(\bar{u}_1)}\,\sqrt{I(\bar{u}_2)}} \quad . \qquad (19)$$

To understand how this parameter can help to simplify the problem, consider the case of partial coherence arising from a uniform extended incoherent illumination source. By the VanCittert-Zernike theorem, if the distance between the points $(\bar{u}_1)$ and $(\bar{u}_2)$ is small compared to the

distance to the source, the degree of coherence is given by the normalized Fourier transform of the source intensity distribution. Thus, for a Gaussian source, μ will be Gaussian. For a square source, it will be the two-dimensional sinc functions; for a circular source, it will be the Bessel function of first kind and first order.

Basically then, the degree of coherence of the illumination on the object will be a function only of the difference in coordinates for those cases of interest. Thus the mutual intensity of the object can be written

$$J_o(\bar{u}_1,\bar{u}_2) = \mu_o(\bar{u}_1 - \bar{u}_2) \sqrt{I_o(\bar{u}_1)} \sqrt{I_o(\bar{u}_2)} \quad . \tag{20}$$

That is, we can represent the mutual intensities by two two-dimensional functions: μ and I.

The problem of computing four-dimensional FFTs remains. If Eq. 20 is examined, we see that this representation has terms that are separable by points (the intensity function), and it has a term μ that is normally separable by coordinates (as, for example, with Gaussian or sinc forms for the degree of coherence of the illumination). If the degree of coherence would be approximated by a function that were totally separable in all coordinates, then Eq. 20 could be separated by points into a product of two two-dimensional Fourier transforms which would then split into a product of two two-dimensional transforms, which can be computed easily. Extending this approach, we looked for an approximation for the modulus of μ that was a *sum* of totally separable terms and was a sum only of the absolute values of the difference in terms. To this we added a complex phase that was separable by points, as are the intensity terms in Eq. 20. In each axis, the functions we selected for a cosine series representation of μ are of the form

$$\sum_{n=0}^{N} A_n \cos \frac{\pi q n}{2} (\bar{u}_1 - \bar{u}_2) \quad , \tag{21}$$

where α is a parameter that determines the coherence radius. For example, if α is zero, the functions yield coherent imaging. Many realistic coherence functions can be well represented by such a cosine representation.

Note that this function is separable by expanding the terms using trigonometric identities and that it is symmetric in $\bar{u}_1$ and $\bar{u}_2$. This results in a representation for the mutual coherence of the form

$$J_o(\bar{u}_1,\bar{u}_2) = \sum_{n=1}^{M} f_n(\bar{u}_1)\, f_n(\bar{u}_2)\, e^{i\phi(\bar{u}_1)} \sqrt{I(\bar{u}_1)}\, e^{i\phi(\bar{u}_2)} \sqrt{I(\bar{u}_2)} \quad . \quad (22)$$

Since the optical transmission function also separates, as it is a set of ones and zeros distributed over the aperture, the entire transmission as given by Eq. 18 also separates into a sum of separable functions.

Appendix C gives an example of a six-term cosine series representation of μ (Eq. 21) and of the resulting 121-term separable representation (Eq. 22). The result is plotted in Figure 2.

B. THINNED ARRAY REQUIREMENTS FOR IMAGING

The two viewpoints of imaging discussed above (i.e., the convolution integral and transfer function representations) permit a revealing approach for the application of thinned arrays to imaging systems. To achieve high resolution in the image, the high spatial frequency content of the object must be maintained. Referring to Eq. 6 for the coherent case, we note that a large aperture is required to sample the high spatial frequency content of the object transform field. Relating this requirement to the convolution integral representation (Eq. 1) and recalling the relationship of Eq. 3 between the system impulse function $h(\alpha,\beta)$ and the aperture $P(x',y')$, it is seen that a large aperture implies a sharply peaked system impulse function with low subsidiary sidelobe levels. In this case, the contribution to the image field intensity distribution will be given mainly by the sharply peaked mainlobe of the aperture, with relatively small contributions coming from the low-level sidelobes in the convolution process.

For the incoherent case, similar interpretations can be given, although the aperture (or pupil function) $P(x',y')$ appears now in a less

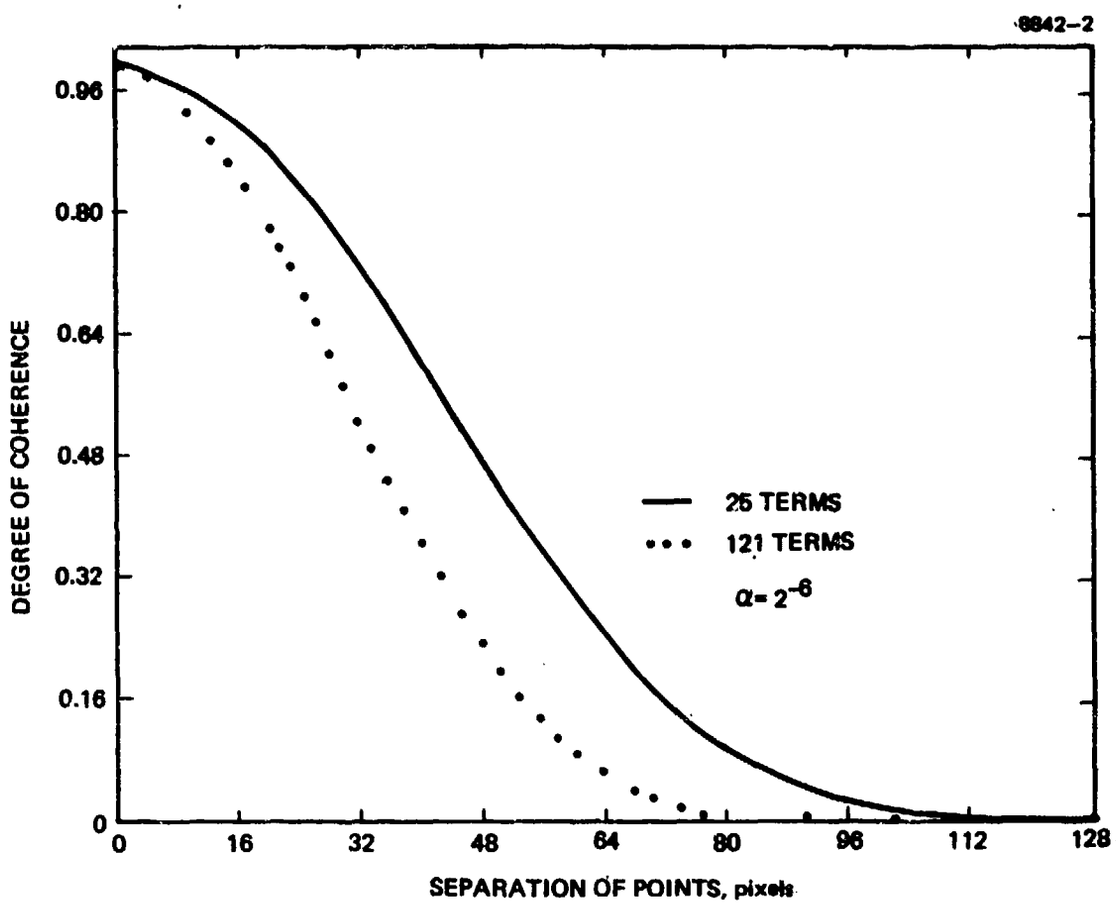

Figure 2. One axis separable degree of coherence. The two-axis function is a product of one-axis functions.

direct way through the system impulse function $|h(\alpha,\beta)|^2$, which represents the received power distribution of the array pattern. Again, referring to the transfer function representation (Eq. 8) and recalling the autocorrelation relation of the aperture to the OTF $\tilde{H}(f_x,f_y)$, Eq. 10, it is seen that high-resolution images require detection at large separations in the spatial frequency plane. This translates again into a large aperture. Viewed from the convolution integral diffraction point of view, Eq. 7, the system impulse function (or point spread function) $|h|^2$ must possess a sharply peaked mainlobe with relatively low level sidelobes. In such a case, the subsidiary sidelobe contributions will not be significant in the convolution integral and therefore will not appreciably degrade the image.

As pointed out in Section 1, high-resolution imaging systems may be infeasible because of the large apertures required. The necessity of utilizing a much smaller number of elements to accomplish the requirements of the full aperture is obvious. Stated most simply, the task is to design thinned arrays that possess the desired characteristics of large apertures for high-resolution imaging applications: sharply peaked mainlobe, low-level sidelobes, and high directive gain.

One obvious way of reducing the number of elements required by a full array while still recovering the total information content of the object is to impose the sampling theorem. Sampling in the aperture plane with a periodic array of receiver elements reproduces an image of the object that is replicated at a distance inversely proportional to the sampling spacing. Spacing the sampling locations at the reciprocal of the object dimension and scaling appropriately for wavelength and target range cause the replicas to just touch. This is the sampling interval dictated by the sampling theorem. Spacing at finer intervals spreads the replicas farther apart, thereby reducing the so-called aliasing effect. However, this is achieved at the expense of requiring more array elements, while not increasing the information content of the image. By truncating the sampled space, each replica has the edge ringing that even a full diffraction limited finite aperture would suffer.

These properties can be demonstrated by defining the convenient sampling function commonly called the comb(x,a), which is $|a|\Sigma\delta(x - na)$. The comb samples a function at the values $x = na$ when it is multiplied by that function. In addition, convolving the comb with a function f(x) replicates that function at the interval a:

$$(1/a)\text{comb}\ (x,a) \circledast f(x) = \Sigma f(x - na),$$

where, for convenience, $\circledast$ represents convolution. The replicas may overlap depending on the extent of the function compared to the interval a. The Fourier transform of a comb is another (reciprocal) comb. As may be recalled from the relationship between grating periodicity and grating lobes or orders in diffraction theory, the Fourier transform of comb (x,a) is

$$\widetilde{\text{comb}}\left(x', \frac{1}{a}\right) = \Sigma\delta(x' - n/a) \quad .$$

By the convolution theorem, if a sampled function is Fourier transformed, then a replicated transform of the function is produced:

$$\text{Fourier transform of}\left[\widetilde{\text{comb}}\left(x', \frac{1}{a}\right)\ \tilde{f}(x')\right] = f(x) \circledast \text{comb}(x,a) \ .$$

Because of the reciprocal nature of the transformed comb, the closer the original samples, the farther apart are the replicas in the convoluted transform. If an object f(x) is bounded at x_{max}, then its replicas will just touch if the object transform $\tilde{f}(x')$ is sampled at $a = 1/x_{max}$. Finer sampling of the object's transform $\tilde{f}(x')$ spreads the replicas apart. This may be viewed, in the case of the imaging problem, as spreading apart the grating lobes (the convolution comb) of the aperture array (the sampling comb). Limiting the required infinite number of samples needed for exact reproduction of each replica to a sample of finite extent distorts the reproduction in exactly the same way as does a truncated full aperture (i.e., continuous sampling). It produces all the well known distortions and edge "ringing" of diffraction by a truncated aperture. The number of sampling points required equals the

number of resolution elements seen on the object. For the coherent case, the number of sampling points is, in fact, the number of elements in the array; for the incoherent case, each sampling point is derived from a pair of elements. N elements provide N(N-1)/2 pairs including possible redundancies.

In determining the best thinned array configurations for high-resolution imaging, the vast amount of established analysis of antenna array theory can be fruitfully applied to imaging systems. In particular, the concept of random arrays appears to be an optimum approach to this problem. Although random arrays have been analyzed in detail for use in microwave antenna theory, their utilization has been restricted mainly to signal detection in the microwave region. To the best of our knowledge, their application to imaging systems has not been explored. The properties of random arrays and their superiority for high-resolution imaging applications are discussed in the next section.

C. THINNED RANDOM ARRAYS

As discussed previously, the problems associated with the implementation of high-resolution image systems (whether full arrays, uniformly thinned arrays, or algorithmically designed thinned arrays) may be alleviated by using thinned random arrays. Random arrays offer distinct advantages over conventional arrays not only in their ability to accomplish the objectives of the imaging system with many fewer elements, but, perhaps equally important, also in their ability to predict the a priori probability of a successful design. The mathematical details of the properties of random arrays have been investigated by Lo as they apply to antenna theory. Some essential results of this work are reproduced in Appendix A. Although this theory has been well developed for antenna applications, its usage in imaging systems has not been explored (as evidenced by a search of the published literature). The many attractive advantages of this class of thinned arrays are discussed below as they apply to high-resolution imaging systems.

Random arrays can achieve high resolution, low sidelobes, and high directive gain with only a small fraction of the number of array elements normally required by uniform arrays to accomplish the same objectives. Furthermore, the fraction of reduction possible (i.e., thinning factor) becomes more dramatic as the number of elements normally required in the uniform array increases. For this class of arrays, the sidelobe levels are closely related to the number of elements used in the array and, to a much lesser degree, to the aperture dimension. Steinberg has concluded that the peak sidelobe level is linearly dependent on N, the number of array elements, and only logarithmically dependent on the aperture dimension. Therefore, for a given number of elements, higher and higher resolutions can be obtained by spreading these elements over a larger and larger aperture; the sidelobe levels would remain substantially the same while the mainlobe is narrowed proportionately. On the other hand, if the array aperture size is fixed, the required specifications of the array can be attained with many fewer elements by using random arrays. As few as 15 elements will give good agreement to theory under certain conditions.

Equally important, the question of the successful realization of a design to prescribed specifications must be considered. Since no general theory exists for the algorithmic design of aperiodic arrays to meet prescribed performance levels, the results must necessarily be obtained by a trial-and-error procedure, even with the aid of high-speed computers. Contrast this with random arrays, which give an a priori probability of success in meeting design specifications. The probability of success is determined before any detailed computations are carried out.

Although the properties of random arrays are approached from a probabilistic point of view, the performance of the array is not probabilistic. The performance of the array is completely deterministic once the disposition of the array elements has been decided. Thus, in this approach, the design of an array is reduced to playing a game of chance, for which the odds in favor of success could be designed to be overwhelmingly in our favor. For one-dimensional arrays, experimental

verification of these characteristics have been made on antenna patterns in the microwave region by Lo and Simcoe. The agreement between experiment and theory was remarkable. Similarly, Steinberg has compared the peak sidelobe levels between random arrays and algorithmically designed aperiodic arrays. Specifically, he compared 70 algorithmic arrays with 170 random arrays for the distribution of their peak sidelobes. He found that both distributions were nearly log normal with the same average and median values. However, a crucial difference existed in their standard deviations. The standard deviation of the random array's distribution was found to be approximately half that of the algorithmic array's. Thus, "the compactness of the random distribution almost guarantees against selection of a random array with catastrophically large peak sidelobes."

Other significant advantages exist for random arrays. Because many fewer elements are required in one mode of application of random arrays, the rate of transmission of information from such arrays would be less than that required for full or uniform arrays, thereby reducing the bandwidth of the transmission. The tolerances on the exact disposition of the array elements need not be very stringent for random arrays to achieve the design specifications. Recognizing the fact that the sidelobes of random arrays are disposed at random locations relative to the mainlobe, there exists a very simple scheme of image enhancement to suppress the spurious background levels caused by the sidelobes. By averaging the reconstructed images obtained from different random array configurations, the background levels can be suppressed as $1/\sqrt{M}$, where M is the number of images used for the averaging process. The different array configurations can be achieved through the use of reflector elements placed at various locations, and the signals from these reflectors can be transmitted to the receiver elements through a switching sequence. Finally, by the very nature of the random array concept, the performance of these arrays is not very susceptible to individual array element failures or destruction. Subsets of larger random-array configurations will perform adequately without catastrophic effects. This graceful degradation is shown in the computer simulation results in Section 2.D.

The incoherent OTF of the thin random array, which can be calculated by its autocorrelation, will have very few redundant vector spacings (see Figures 5, 7, and 8). There are N(N-1)/2 vector spacings produced by N array elements. For incoherent imaging, these spacings in autocorrelation space are the spatial frequency sampling points. The OTF measures the existence and number or redundancy of these samples as a function of spatial frequency. If it were possible to sample fully and have no redundancy at all, then it would require approximately only $\sqrt{2N}$ array elements to have N desired unique samples. The full array of N elements can distinguish N unique resolution elements in its FOV. This may be seen by noting that the FOV of the array is determined by the diffraction angle of the array element and is inversely proportional to the element dimension while resolution is proportional to array dimension. For example, for a 4096-element full array, only $\sqrt{2N} \sim 91$ elements or $\sqrt{2/N} \sim 2\%$ of the full array would be required for complete sampling were it not for occasional redundancies and missing spatial frequencies. More elements are needed to make up the deficiency. In one dimension, there are only a very few nonredundant arrays possible. In two dimensions, it is impossible, in principle, to have a nonredundant array that fills the autocorrelation space of the array. In our studies for monochromatic imaging, we have found it necessary to employ random array elements only three times more numerous than this theoretically unattainable nonredundant design number. For polychromatic imaging (as explained below), only 1.5 times more was needed. Thus, thinned random arrays can automatically perform low redundancy sampling.

The above discussion has concerned monochromatic or quasi-monochromatic radiation. For polychromatic incoherent imaging, even fewer elements are needed in the thinner array to get a good sampling of the spatial frequency plane. Each array element pair defines or measures a different spatial frequency for each different wavelength, so many new spatial frequencies are sampled as the bandwidth is increased. If the object does not have a pathologic spatial frequency-"color" relationship, polychromatic imaging with a thin random array will be superior to monochromatic. Our computer simulations bear this out strikingly.

Another class of arrays may be specially constructed to be minimally redundant or even nonredundant and compact up to a maximum spatial frequency that is, however, much less than that given by the maximum dimension of the array (see Figure 10). This class of arrays shares some properties with random arrays, but, since they are generated algorithmically, it is not proper to call them random. These two classes of arrays can be relatively immune, in a special sense, to phase aberrations.

To see how this immunity may come about, consider a pair of aperture elements at a fixed spacing that defines a certain spatial frequency, f, as the elements of an interferometer producing fringes of a certain "visibility." The MTF of the aperture is a synthesis of the visibilities of all such pairs for all frequencies. Adding an additional redundant pair at a frequency f, in the absence of phase distortion, always enhances the MTF at that frequency. But consider an additional pair at f translated somewhere in the aperture where it suff rs a relative space variant phase distortion due to the atmosphere or distortion in figure. It still, as a pair, produces fringes of the same visibility although the fringes are shifted. That is, they are shifted in phase. Synthesizing this pair with the original pair now produces a lesser resultant in the MTF than it would in the absence of distortion and produces possibly even a reduction over that produced by the single pair. On the average, assuming random phases, the growth of the MTF, before normalization, for N contributing pairs of elements would be as in random walk (i.e., proportional to $\sqrt{N}$). But, since the normalization at zero frequency reduces the entire transfer function by 1/N, the net result is a $1/\sqrt{N}$ reduction in the MTF at that spatial frequency. For nonrandom phase disturbances, the MTF may become very small, or, in some cases, negative. Clearly, nonredundant or minimally redundant arrays would not suffer significantly from these problems. Radio astronomers have been interested in this possibility. It remains to be decided by experiment whether, in the presence of space variant phase distortion, it is more desirable, with respect to given image quality criteria for given classes of images, to have the arbitrary sampling of space varying phase in the thin array rather than to have the average but distorted phase in

the full array. One such comparison experiment is described in Section 2.E.2.

D. SIMULATION PROCEDURE

Computer simulation studies of random array imaging were carried out for the incoherent, coherent, polychromatic incoherent, and partialy coherent cases. A modular software package was designed for use on the simulation studies. This approach was taken to provide a flexible single executive control program that would simulate these cases while allowing optional system parameters to be introduced as needed. These optional system parameters include Gaussian or Poisson noise, atmospheric turbulence, aperture configuration, and percent thinning factor in the thinned random arrays. Additionally, the output format of the reconstructed image and pertinent intermediate data files can be chosen to be in floating point or packed integer arrays, the latter with or without a header. A block diagram of the simulation software package is shown in Figure 3.

The simulations are based on the Fourier representations of the incoherent and coherent imaging process, shown by Eqs. 4 and 8. The basic components of the simulation are a Fourier transform of the digitized object array (i.e., the input image), OTF corresponding to either the incoherent or coherent case, and an inverse transform of the product of the above two components to reconstruct the object (i.e., the reconstructed image). Additional components of the simulation are incorporated, as needed, to determine the influence of system parameters on image quality. The sequence of operations that takes place in the simulations is described below.

For the coherent imaging case, a random phase of range 0 to 2π is first multiplied on a pixel-to-pixel basis to the digitized input image. This simulates the effect of speckle, which appears in coherently illuminated objects. The transformation of the input image to the far-field, or aperture, plane is accomplished by taking a fast Fourier transformation of the input image. At this point, an aperture configuration is generated that consists of a binary pattern of regular or random array

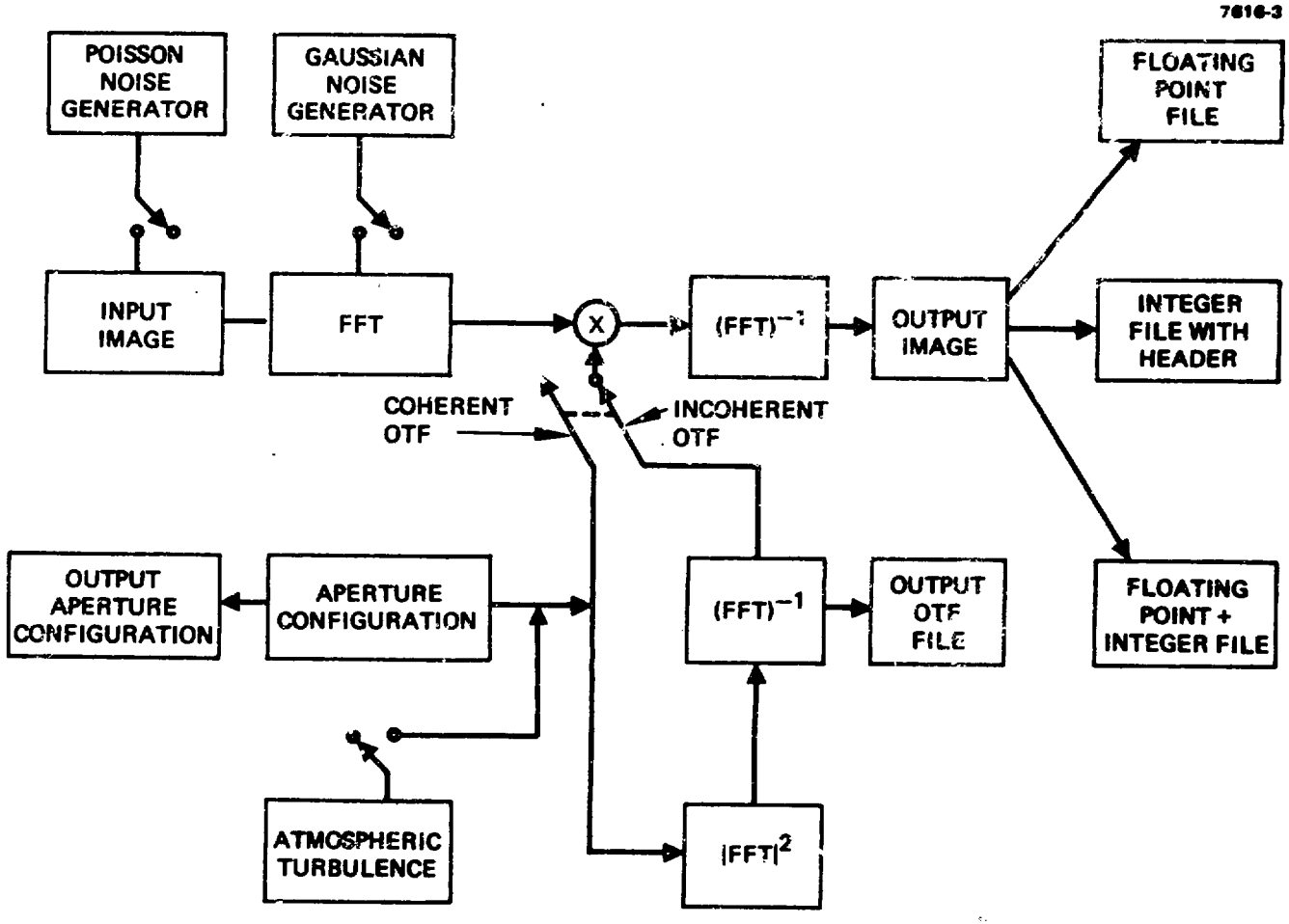

Figure 3. Block diagram of simulation scheme for coherent and incoherent imaging.

elements. Examples of regular and random array patterns are shown in Figure 4. The patterns are represented in binary form, with bright pixels corresponding to a value of 1 and dark pixels to a value of 0. A value of 1 in the aperture configuration represents a point where an antenna element in the array exists, and a value of 0 represents the absence of an antenna element. The aperture plane spatial frequencies are sampled only at those locations where an antenna element exists (i.e., where the antenna configuration is represented by a 1 in the binary array). The product of the Fourier transform of the input image with the aperture configuration, taken on a pixel-by-pixel basis, then produces the Fourier representation of the reconstructed image. Finally, an inverse Fourier transform of this product array produces the reconstructed image, as imaged with the corresponding antenna array configuration.

For the incoherent imaging case, there exist two major differences in the simulation procedure. First, there is no complex random phase associated with the input image because an incoherently illuminated object produces only an intensity distribution across the object. All phase information is suppressed. The fast Fourier transform is taken with respect to the intensity distribution of the input image only. Second, the OTF for the incoherent case is no longer a binary array representative of the antenna configuration above. For incoherent imaging, the OTF is derived by taking a Fourier transform of the aperture configuration, then a complex absolute value squared of this Fourier transform, and finally a second Fourier transform of this function. In coordinate space, this is equivalent to taking an autocorrelation of the aperture configuration. Thus, the spatial frequencies in the aperture plane are sampled by pairs of antenna array elements, with the sampled spatial frequencies represented by vector distances between all possible pairs of elements in the array. Thus, depending on the aperture configuration, redundant sampling is likely to occur. With the exception of the above two differences, the simulation scheme for coherent and incoherent imaging is identical.

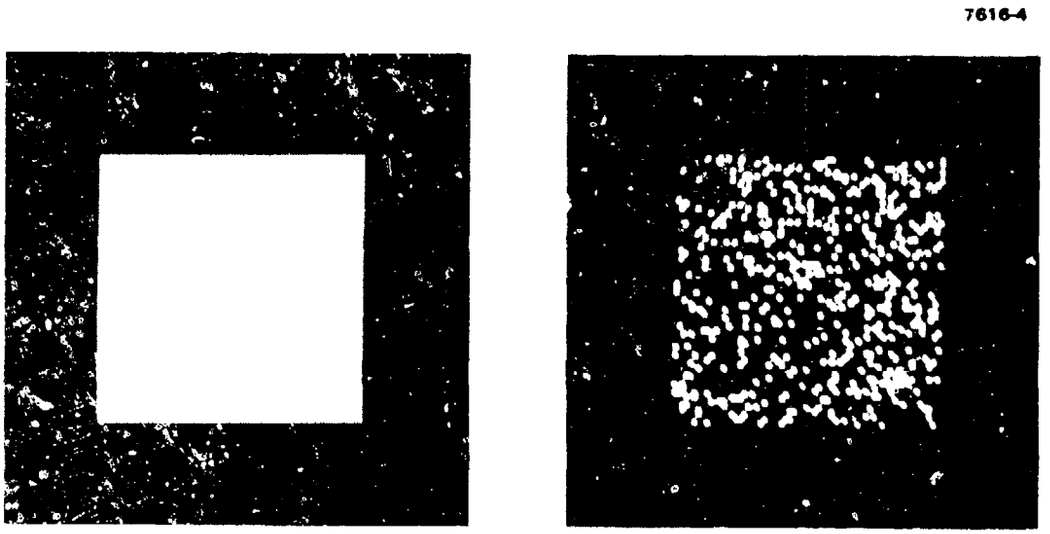

Figure 4. Representative aperture configurations.

The incoherent MTF of a full 64^2 square aperture is shown in Figure 5. Note the high peak (large redundancy) plotted in the center of the pattern at zero spatial frequency and the general fall-off until the aperture-limited frequency is reached. The PSF of this full square array is shown in Figure 6 and exhibits the familiar sinc^2 behavior. For comparison, the MTF of a random array of 12.5% of the 64^2 elements is shown in Figure 7(a and b). Only the central 64^2 is plotted there. Note that, except for the central peak at zero frequency, the spatial frequency plane is almost fully uniformly sampled with the low redundancy. Although not shown here, the sampling continues to the boundary. The MTF of a 100-element random array (2.44%) is shown in Figure 8 plotted in slightly more than one quadrant (80^2). Sampling to the boundary is evident here. The PSF of the 12.5% random array is shown in Figure 9. It has a central peak width almost identical to the central peak width of the full array and many additional side peaks of small magnitude. Figure 10 shows the MTF of a small 25-element algorithmically designed array. The MTF is compact and nonredundant up to a small fraction of the frequency domain defined by the full aperture. A more complete sampling is impossible in principle. For minimal redundancy with almost complete sampling, the random array provides an effective design

tion. An illusion makes the region near the center appear to be

'os'.

We have simulated polychromatic incoherent imaging by the process of averaging or overlaying several monochromatic images, each representing a different wavelength. In the simulation, different spectral components were modeled by different overall aperture dimensions. This is legitimate because, in the far field of diffraction, wavelength and aperture size scale directly. For example, if a full aperture of 64 x 64 elements represents 4096 resolution elements at a certain wavelength, then a smaller size 32 x 32 aperture correctly represents the smaller 1024 resolution elements that would obtain from the original 64 x 64 aperture if the original wavelength were made twice as long. The same physical aperture at two different wavelengths can be modeled by two different computer apertures of linear dimensions inverse to the wavelengths.

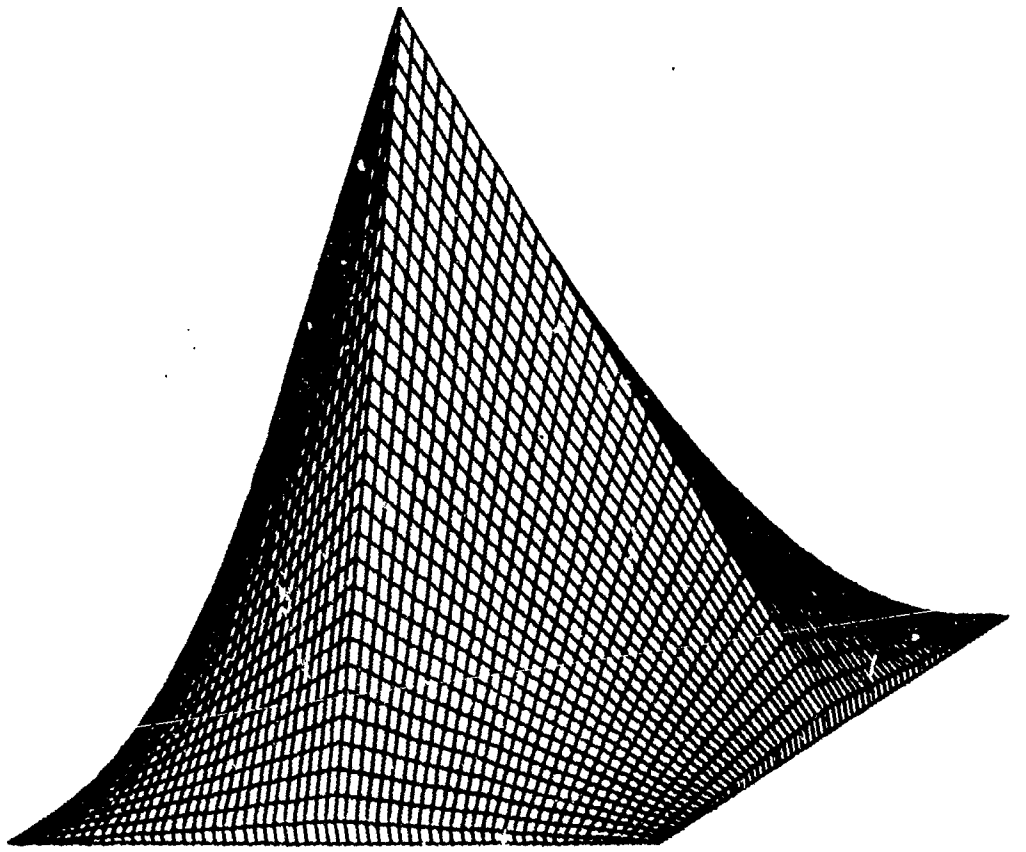

Figure 5. MTF of full 64^2 square aperture.

8842-6

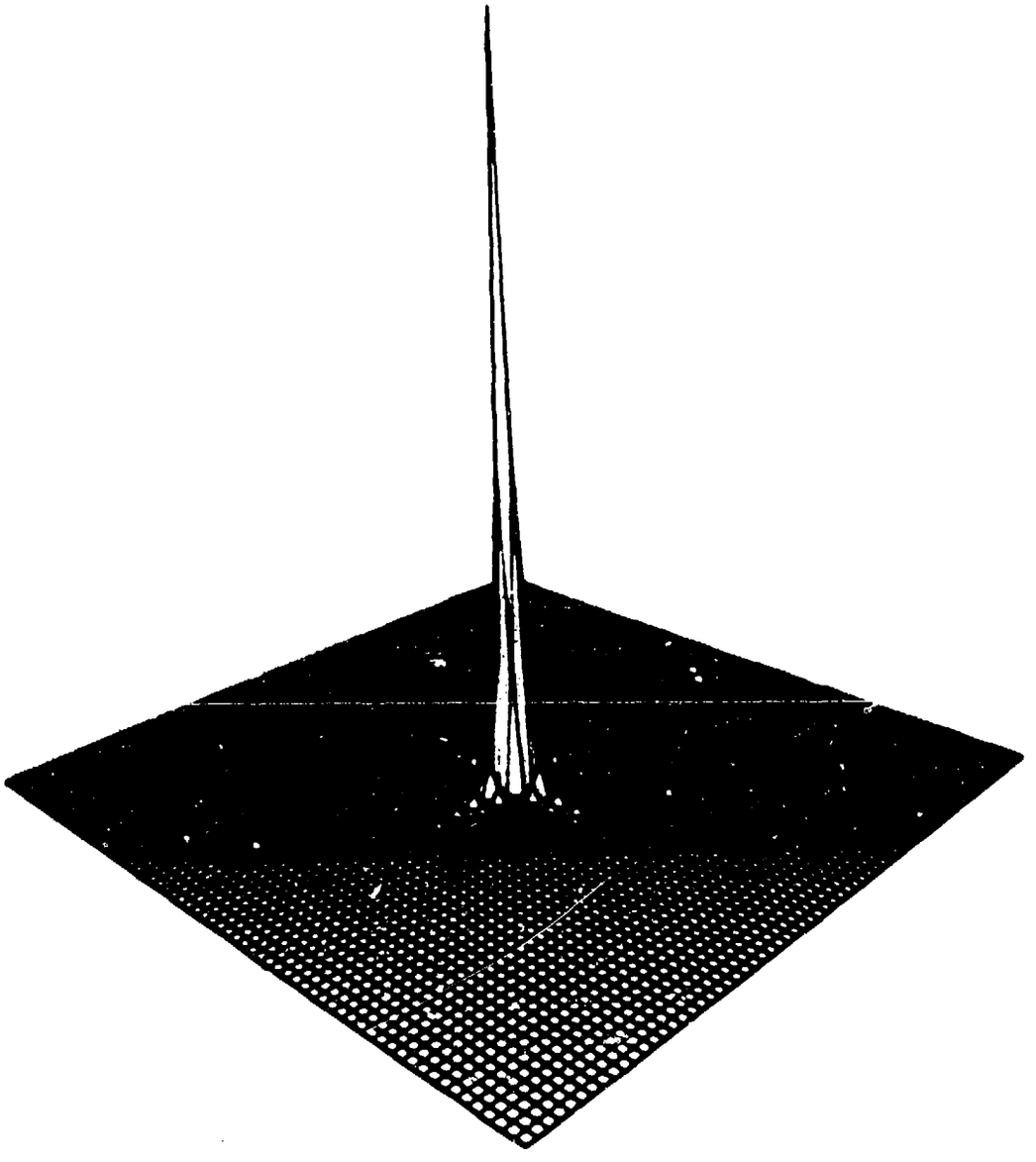

Figure 6. PSF of full 64^2 square aperture.

8842-6

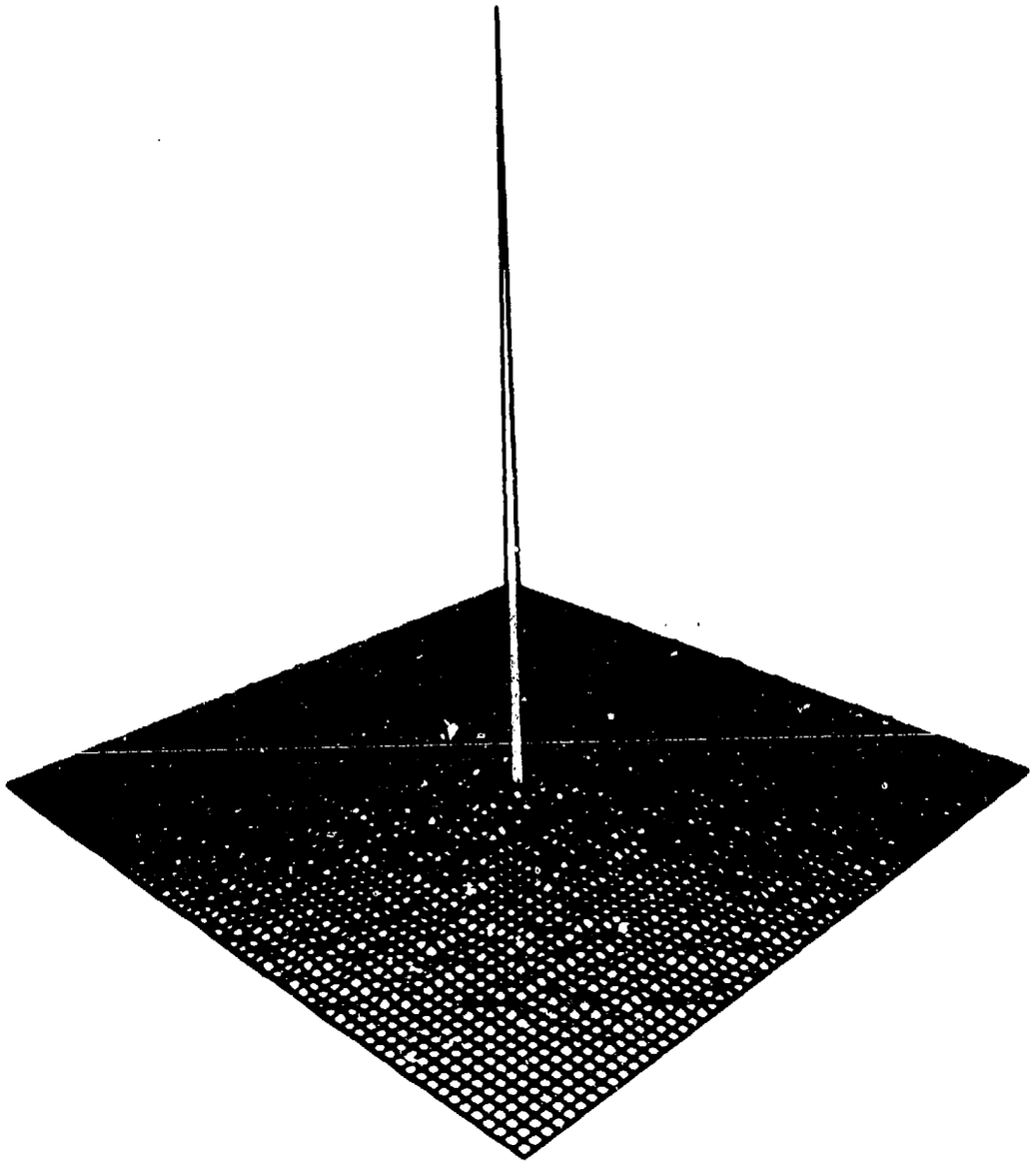

Figure 7(a). MTF of random array of 12.5% of 64^2 elements. Central 64^2 plotted.

8842-4

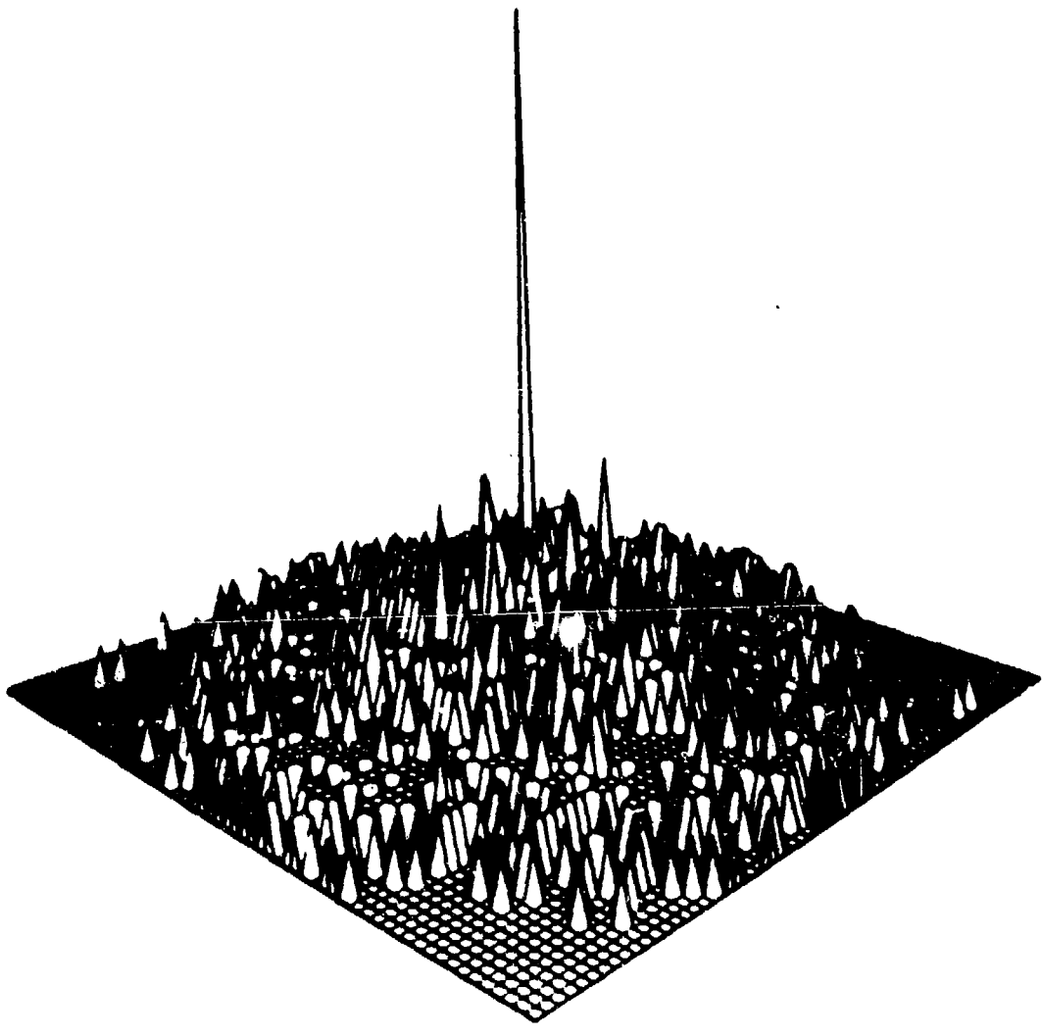

Figure 7(b). MTF of random array of 12.5% of 64^2 elements. Central 64^2 plotted peak clipped.

8842-7

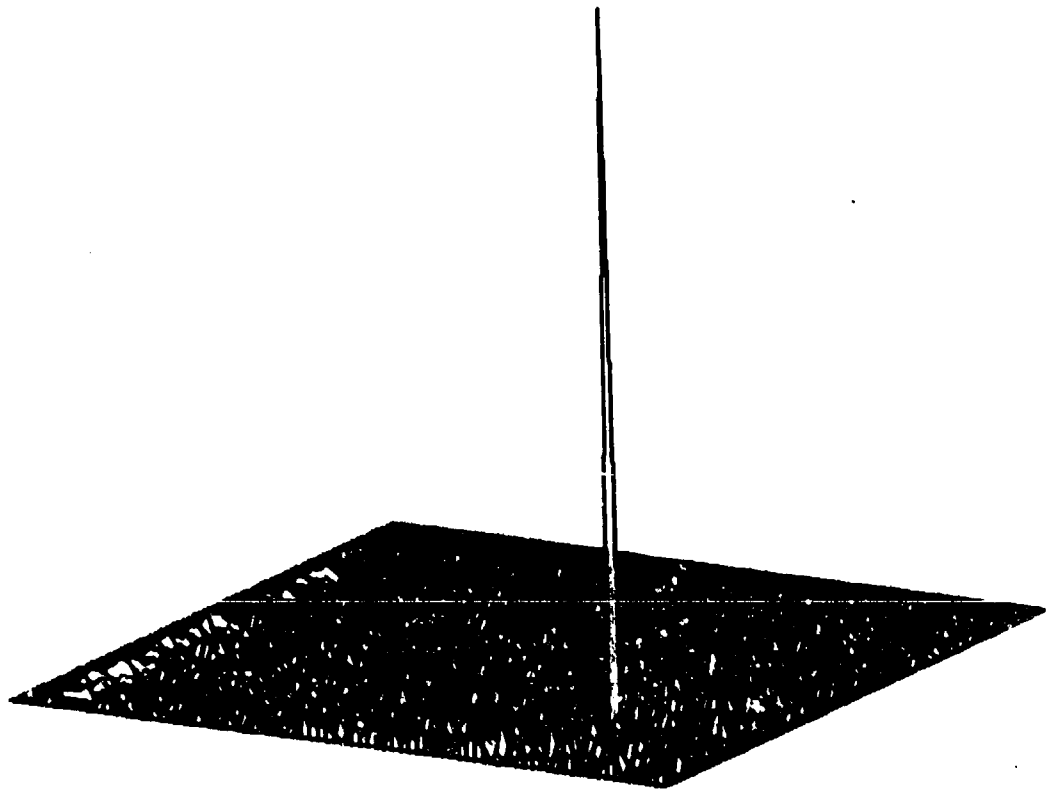

Figure 8. MTF of 100 element (2.44%) random array shown in one quadrant.

8942-8

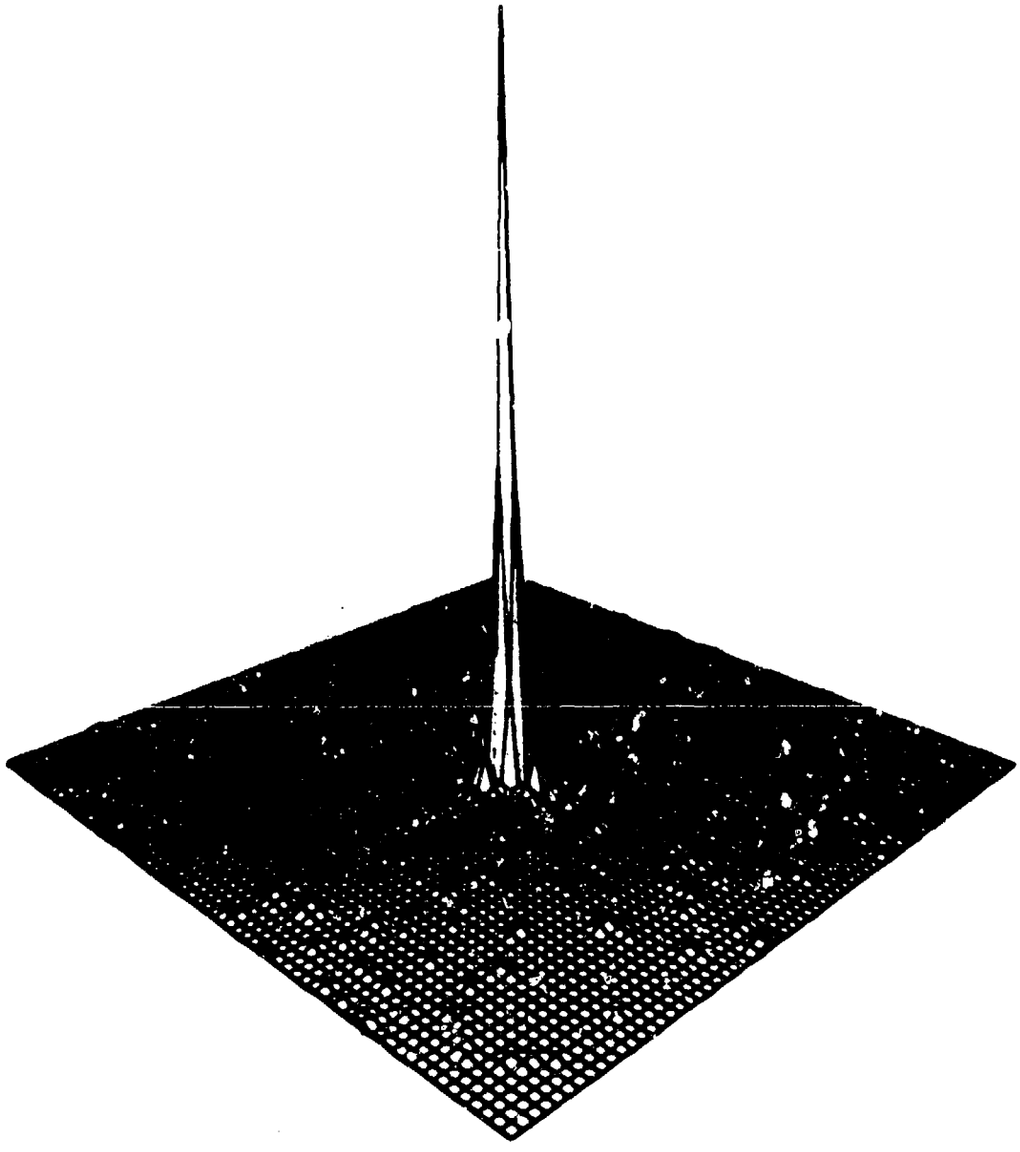

Figure 9. PSF of random array of 12.5% of 64^2 elements.

8842-9

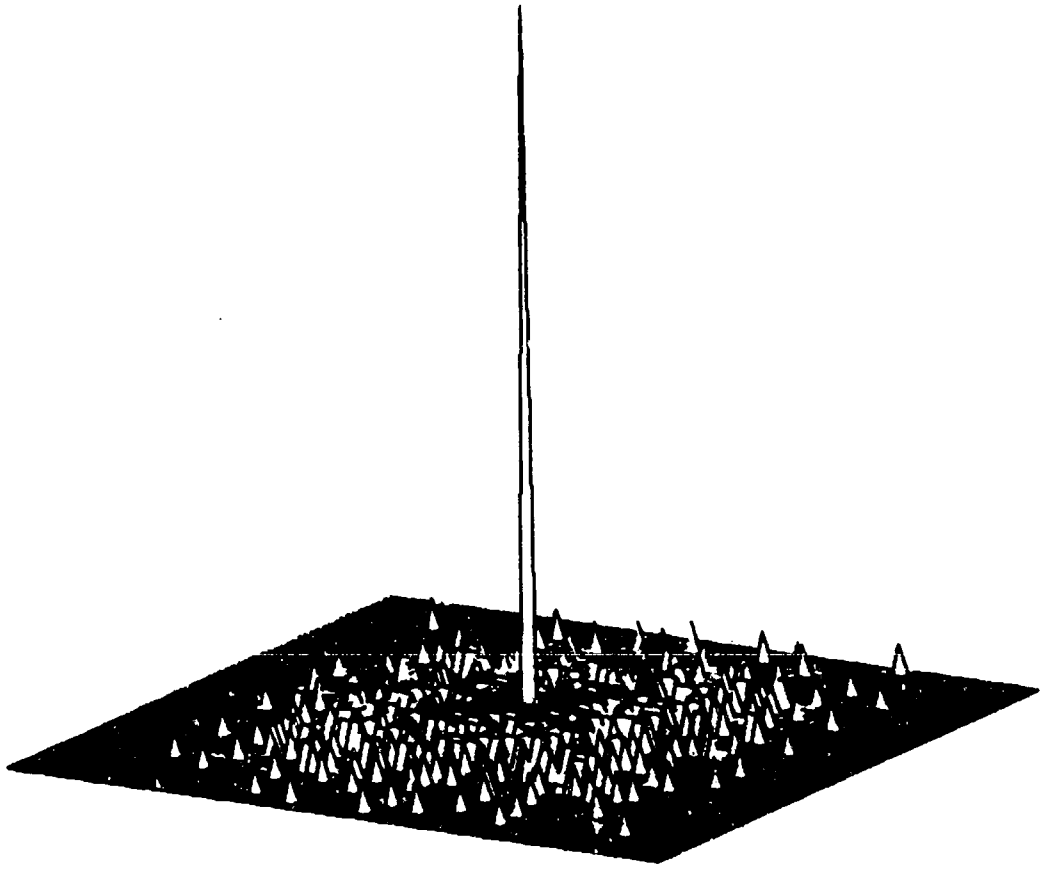

Figure 10. MTF of 25-element nonredundant array.

This is because the physical diffraction angles are determined by the ratio of physical aperture to wavelength. If everything else is physically constant, red light, for example, would have less resolving power than blue.

The sizes of the individual elements in the various apertures we used were kept constant at a single element and positioned at the same relative location while the size of the total aperture was varied. This correctly models the constancy of field of view with changing wavelengths. Each image was renormalized to 8 bits to achieve constant antenna efficiency as a function wavelength. Uniform spectral illumination was assumed in this study.

For the case of partially coherent imaging, the simulation makes use of the specially constructed separable coherence functions described in Section 2.A.3. An arbitrary coherence function may be approximated in this fashion. But if it is not so represented, in separable form, the general four-dimensional convolutions or Fourier transforms that would then be needed would far exceed the computer storage available for 128^2 size images. The computer simulation previously used for coherent and incoherent imaging was modified to accept our separable partially coherent model. A block diagram of this simulation is shown in Figure 11. The procedure is to input an image of 128 x 128 pixels, represented by their intensity values. The square root of each intensity value is taken and, when speckle modeling is desired, converted to a complex number with a random phase factor. This gives us a model for the complex disturbance image. This image was then multiplied by each term in the separable representation of the degree of coherence function μ (Eq. 22), and the Fourier transform was taken of each resultant term. Appendix C gives an example of the terms of such a separable representation for μ. Each term is then multiplied by the optical transfer function for the aperture followed by the inverse transform. The resulting image terms were then squared and added to obtain the output intensity image. Since only the image intensities are of interest, no cross terms are computed, and thus neither the degree of coherence nor mutual coherence of the output image was computed. By this means, the impossible burden of extreme storage needed for four-dimensional computation was transformed to a tractable but lengthy and expensive one.

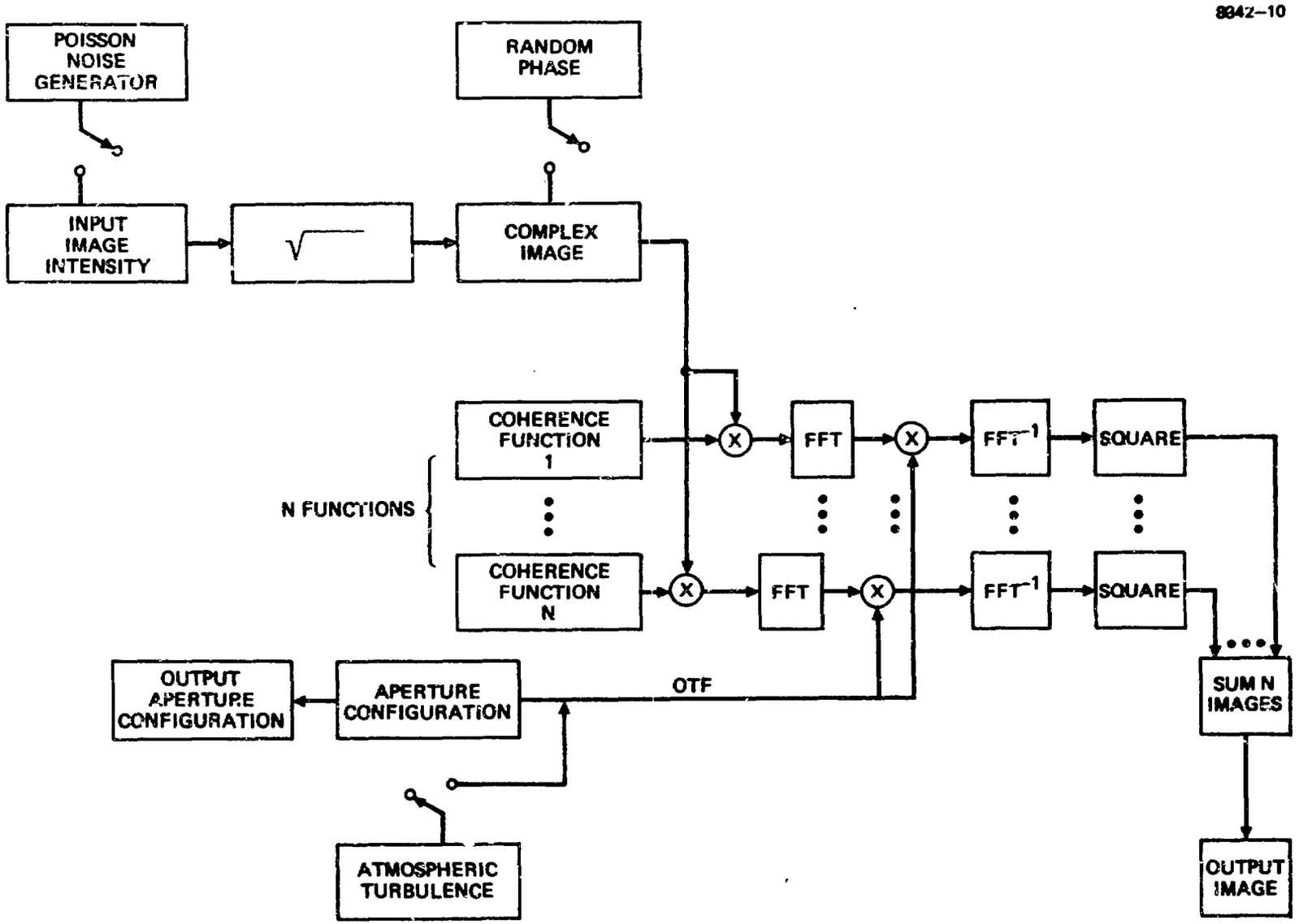

Figure 11. Block diagram of partially coherent simulation.

The aperture configuration used in the simulations is generated straightforwardly. A regular array is generated by setting the antenna element coordinates of a predetermined regular pattern to 1 and the remaining array positions to 0. Generally, a square aperture array configuration was used. For the random array, a random number generator is used to produce the sequence of numbers used as coordinates of the random array elements. Each pair of random numbers forms the (x,y) coordinates of an array element. The random number generator is normalized so that the range of numbers generated falls within the limits of the aperture size chosen.

Additional optional system parameters are available to include in the simulation studies to determine the effect of these parameters on image quality. These include a Poisson noise generator, a Gaussian noise generator, and an atmospheric turbulence generator. The noise generators were used to determine the effect of S/N on image quality for both regular and random array imaging. The turbulence generator was used to determine the immunity, if any, of random arrays to atmospheric turbulence. Finally, there are several options available to output the reconstructed image on disk for display. Either floating point format or integer format is available, with the latter form normalized to 8-bits over the dynamic range of the reconstructed image to display it on gray-scale displays. Options to output the aperture configuration and OTF on disk are also available.

E. RESULTS OF THE SIMULATION STUDIES

Both incoherent, coherent, and partially coherent cases were simulated for monochomatic illumination. Polychromatic incoherent imaging was simulated as well. In these studies, the input image (object) used was a transparency digitized to 8 bits (24 dB) of dynamic range and containing a high background intensity level. This image was digitized to a 128 x 128 pixel array, the limitation on the size of the array being imposed primarily by the core space available in the computer. The size of the largest full aperture was chosen to be 64 x 64 elements centered in the aperture array. With this full array size, the resolution element

in the input image is 2 x 2 pixels in size. A total of $64^2 = 64 \times 64 = 128 \times 128/2 \times 2$ 4096 resolution elements are therefore produced in the full array's FOV. From 128 to 2048 elements were used in the random array simulation studies, corresponding to 3% and 50%, respectively, of the number of full array elements. All random arrays generated in the studies were confined within the 64 x 64 aperture boundary of the full array.

Figures 12 through 16 show the results of incoherent imaging with thinned random arrays. Included in each figure are the object and the full aperture diffraction-limited image. These are shown for comparison with the random array images. Figures 17 through 18 show the results of coherent imaging with thinned random arrays; the corresponding full array image is included for comparison. Because of the onset of speckle effects in coherent imaging, an additional parameter, the number of overlays, is introduced. The effects of speckle can be reduced by speckle averaging, in which reconstructed coherent images with different speckle patterns are added to "smooth out" the individual speckle patterns. The coherent images are shown as a function of the number of overlays used for speckle averaging.

Figure 19 compares full and random arrays for incoherent imaging in the presence of turbulence. Figures 20 through 25 show the results of polychromatic incoherent imaging with thinned random arrays and with the corresponding full array images for comparison. Partially coherent imaging was successfully simulated by modeling the coherence in terms of totally separable functions to avoid four-dimensional transforms, which would have exceeded the storage capabilities of our computer. Nevertheless, the large computational burden precluded more than a cursory examination of the problem. A single partially coherent image required 1 hr of CPU on a PDP KL-10 with a Tenex operating system. Partially coherent, fully coherent, and incoherent images are shown in Figure 26.

1. Incoherent Imaging

The image quality achievable with random arrays thinned to only 12.5% of the number of full aperture elements is shown in Figure 12. Four different configurations of random arrays were arbitrarily chosen,

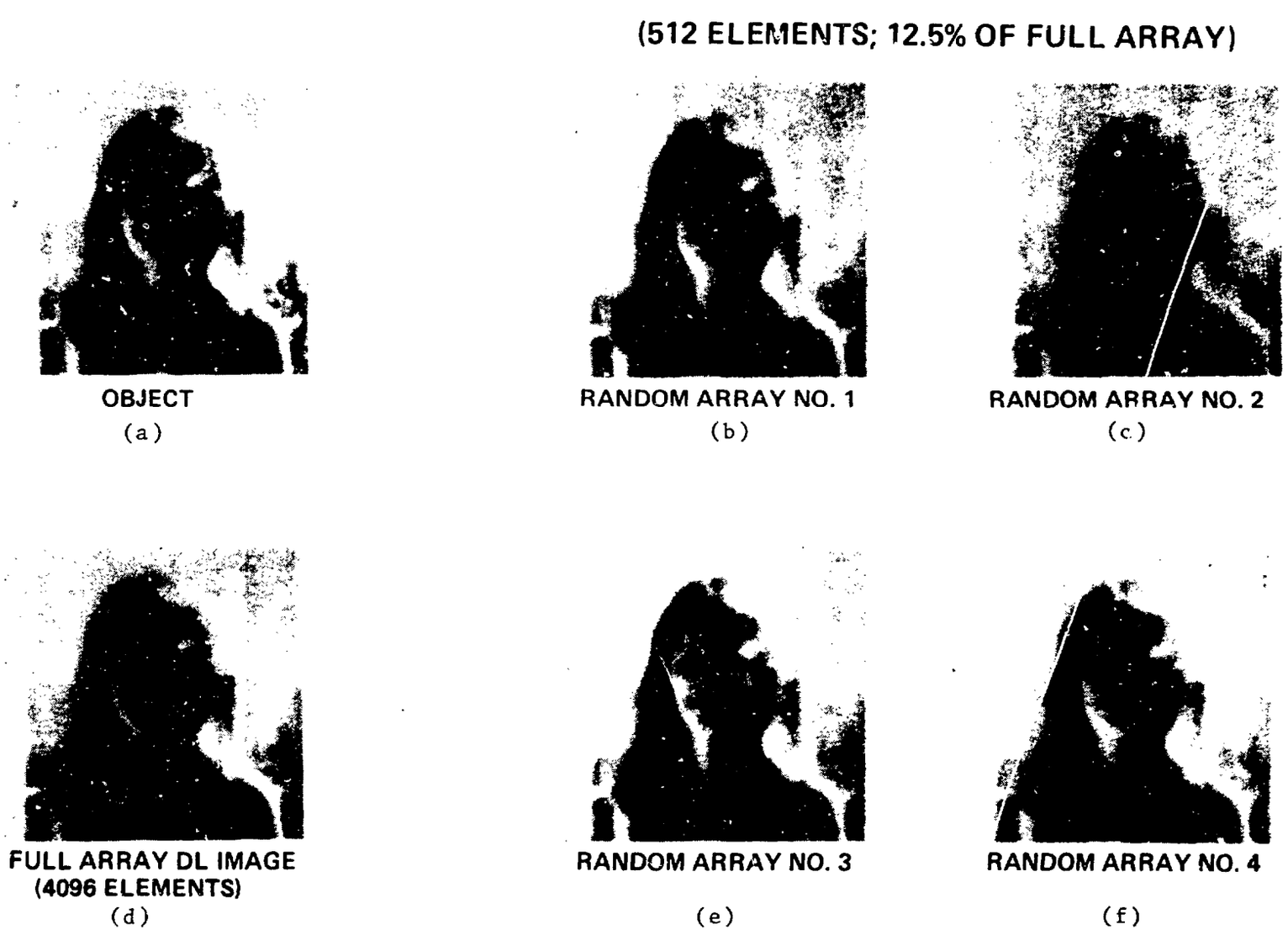

Figure 12. Random array imaging.

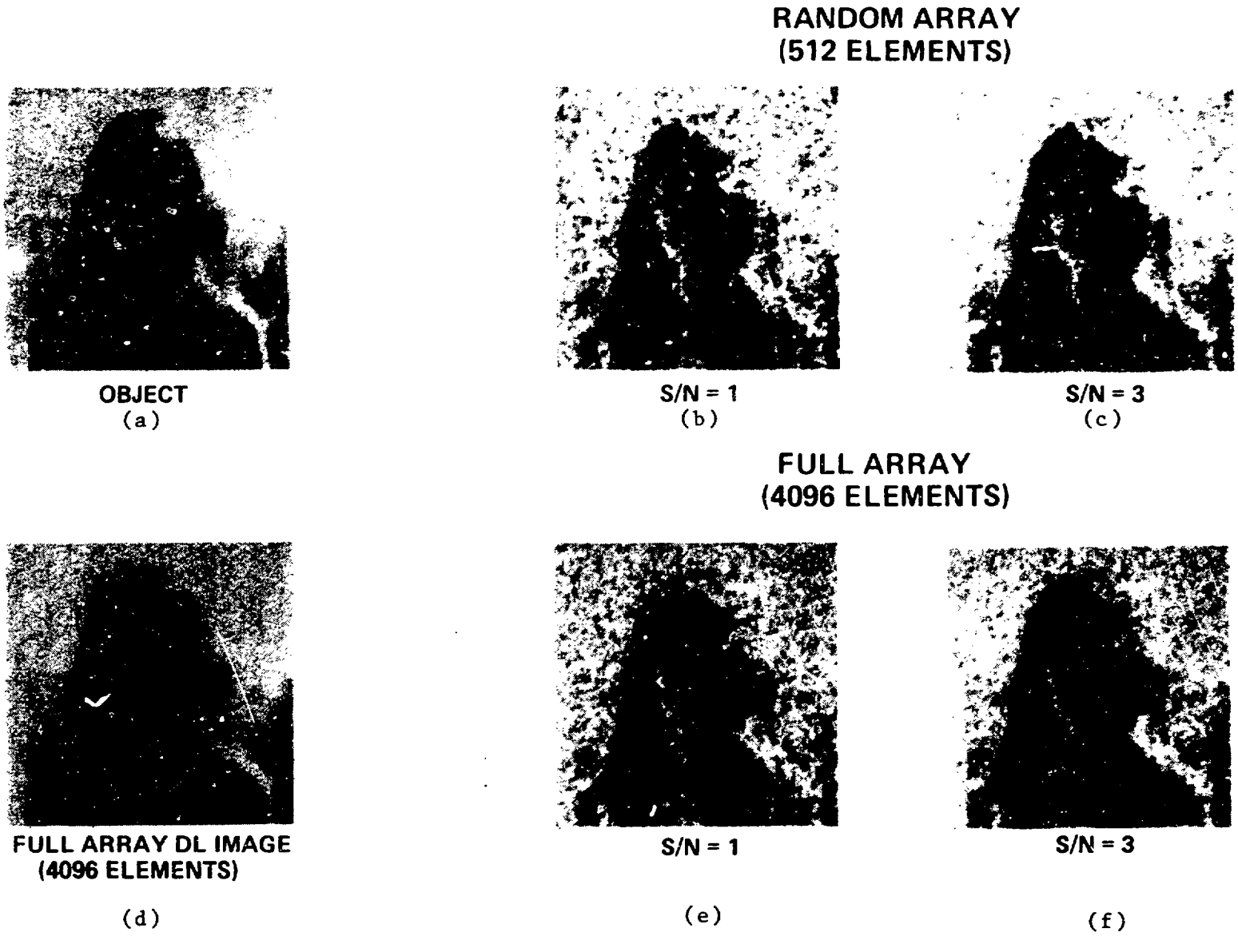

Figure 15. Signal-to-noise ratio.

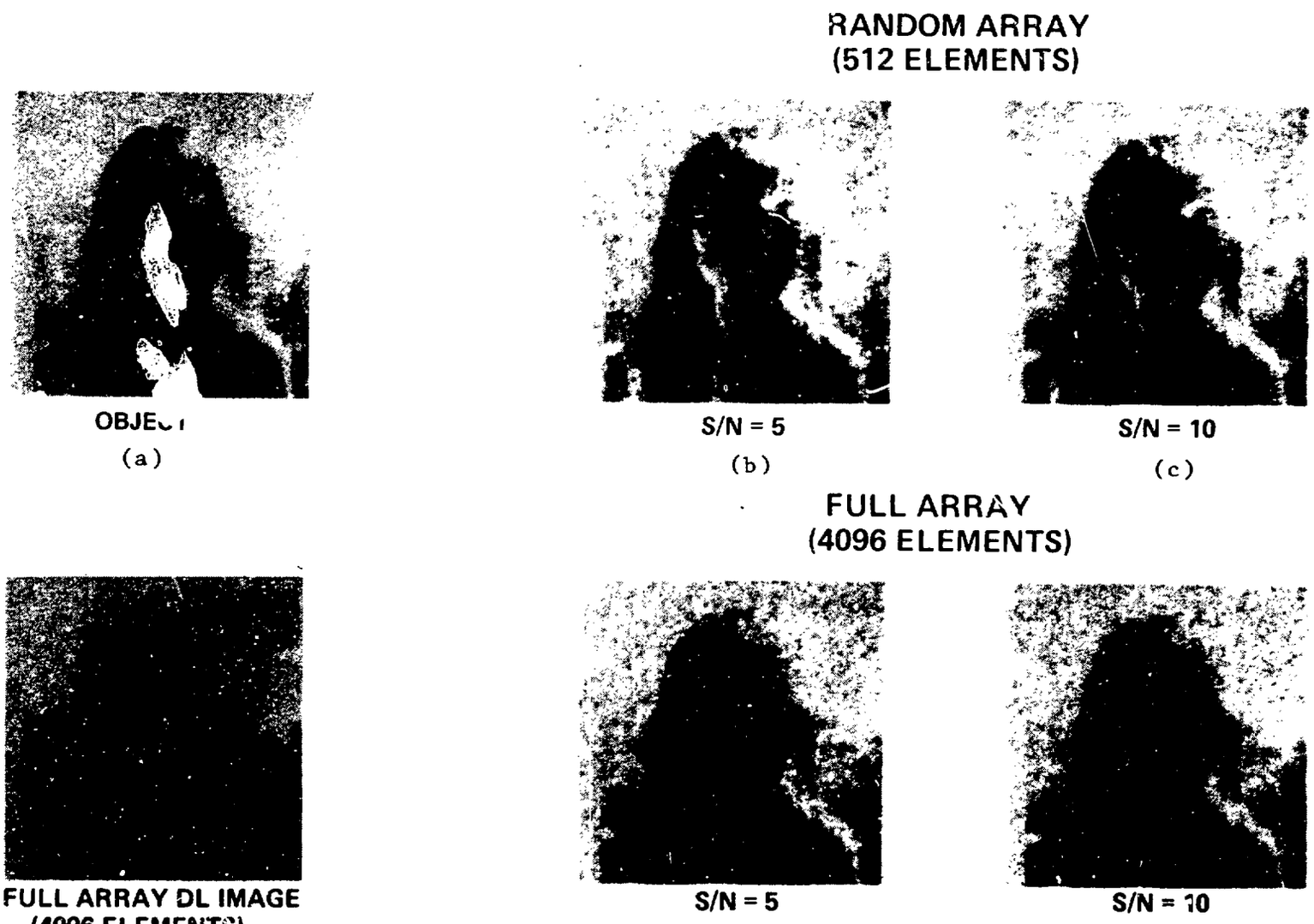

Figure 16. Signal-to-noise ratio.

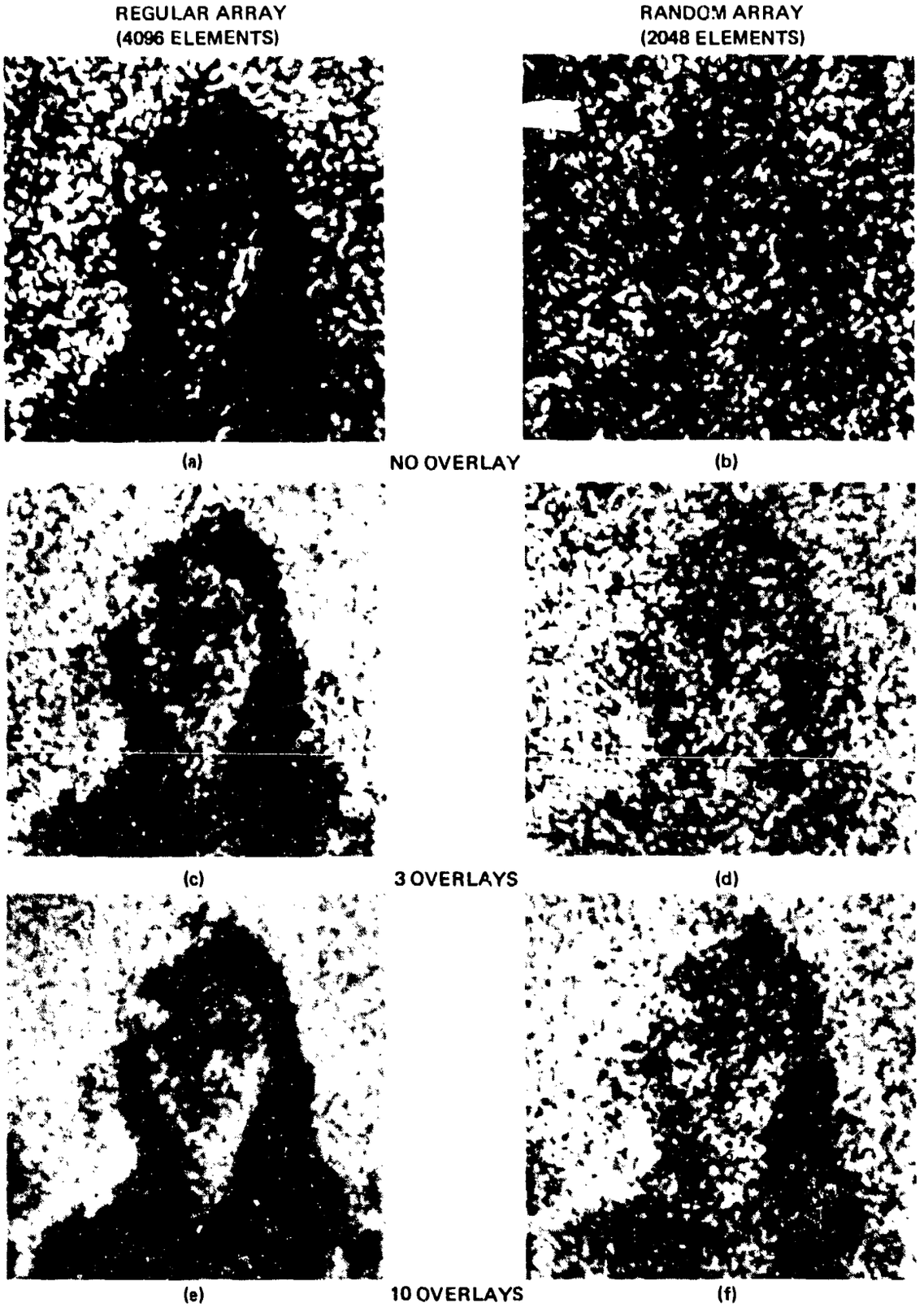

Figure 17. Coherent imaging.

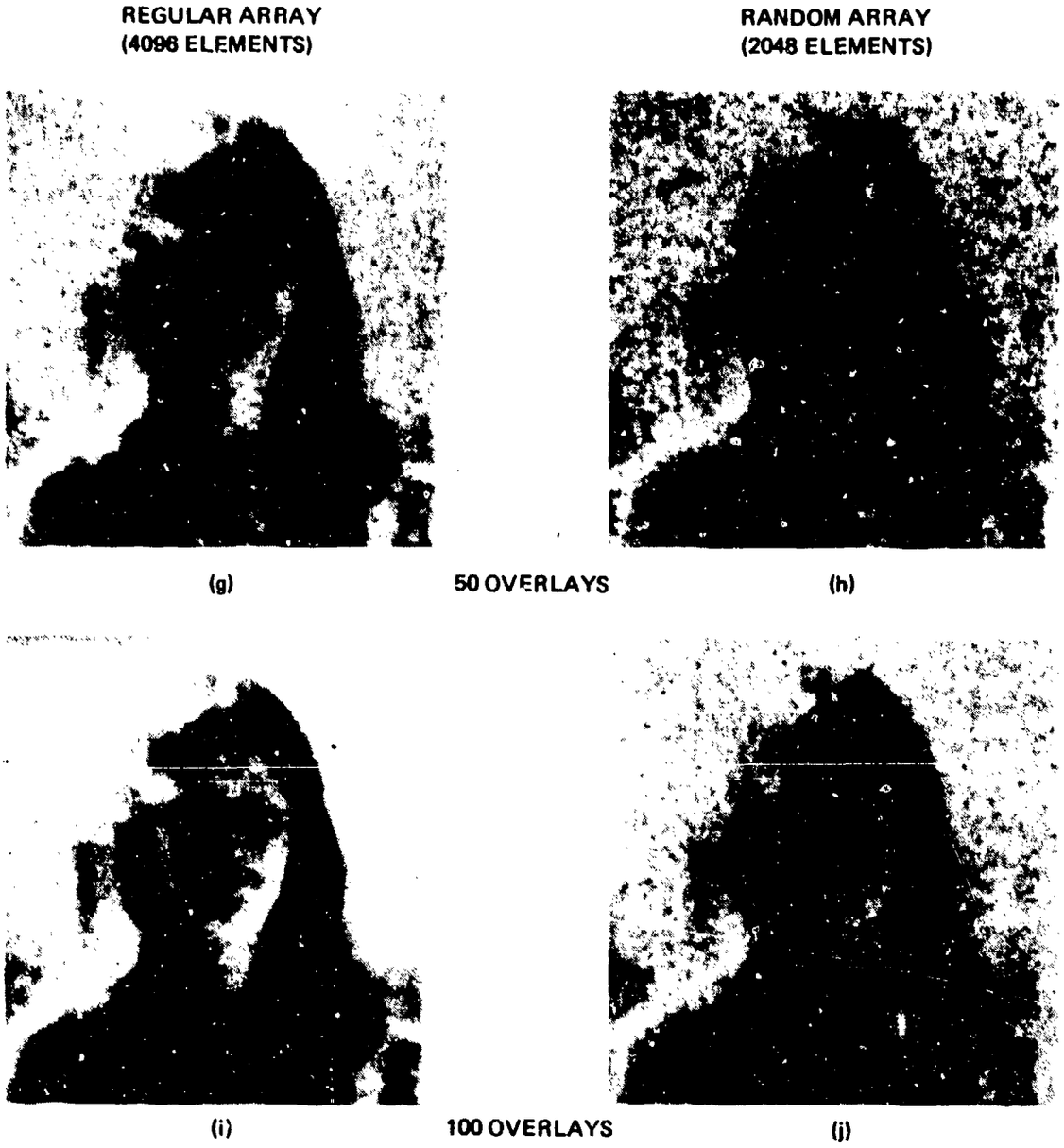

Figure 18. Coherent imaging.

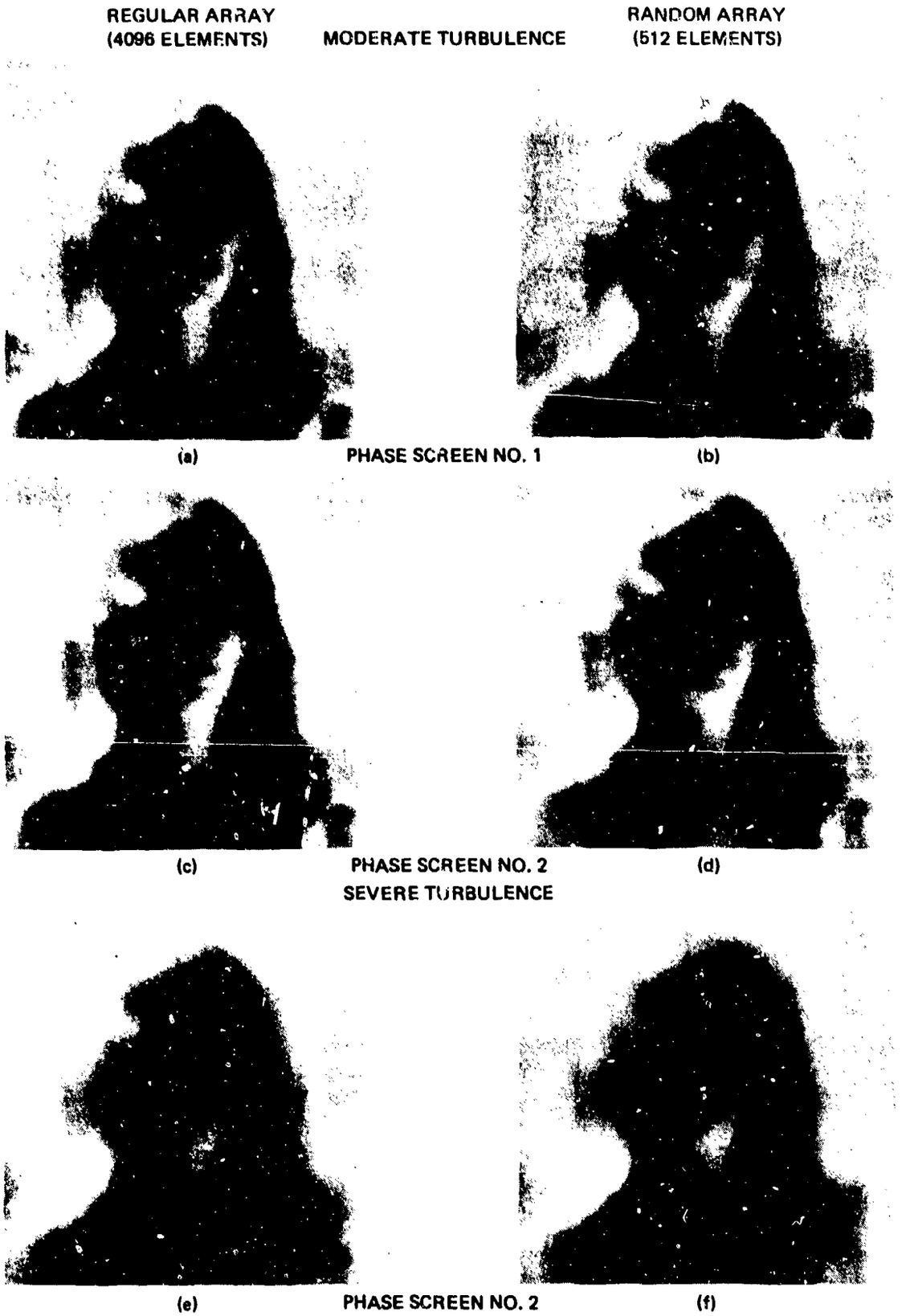

Figure 19. Incoherent imaging in presence of atmospheric turbulence.

8108-1

MONOCHROMATIC DIFFRACTION LIMITED
FULL APERTURE IMAGE

MONOCHROMATIC IMAGE FROM RANDOM
ARRAY NO. 1
25% OF FULL APERTURE IMAGE

ORIGINAL OBJECT

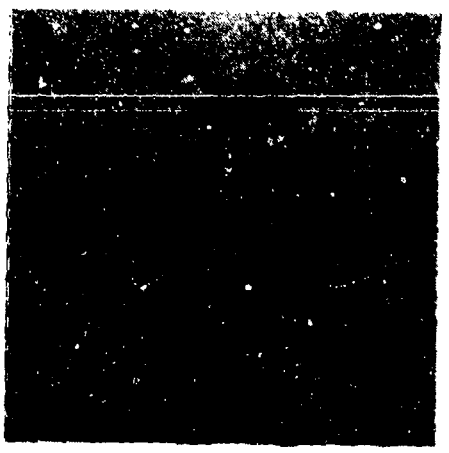

MONOCHROMATIC IMAGE FROM
RANDOM ARRAY NO. 2
25% OF FULL APERTURE IMAGE

Figure 20. Incoherent monochromatic imaging.

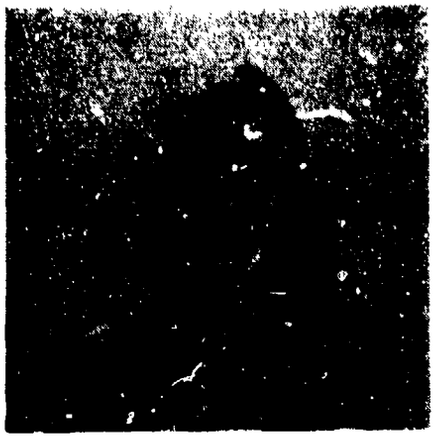

MONOCHROMATIC DIFFRACTION LIMITED
FULL APERTURE IMAGE

RANDOM ARRAY NO. 1
25% OF FULL APERTURE IMAGE

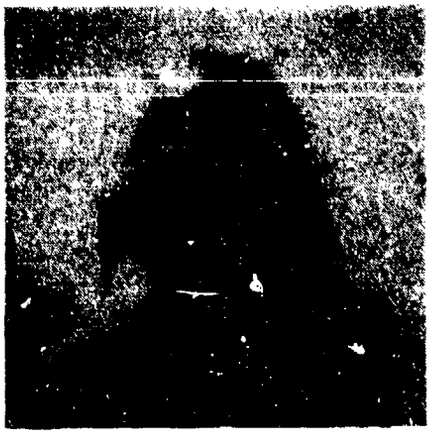

FULL APERTURE IMAGE

RANDOM ARRAY NO. 2
25% OF FULL APERTURE

Figure 21. Incoherent polychromatic imaging, bandwidth span factor 1.14.

8108-3

MONOCHROMATIC DIFFRACTION LIMITED
FULL APERTURE IMAGE

RANDOM ARRAY NO. 1
25% OF FULL APERTURE IMAGE

FULL APERTURE IMAGE

RANDOM ARRAY NO. 2
25% OF FULL APERTURE

Figure 22. Incoherent polychromatic imaging, bandwidth span factor 1.33.

8108–4

MONOCHROMATIC DIFFRACTION LIMITED
FULL APERTURE IMAGE

RANDOM ARRAY NO. 1
25% OF FULL APERTURE IMAGE

FULL APERTURE IMAGE

RANDOM ARRAY NO. 2
25% OF FULL APERTURE IMAGE

Figure 23. Incoherent polychromatic imaging, bandwidth span factor 2.00.

8842–14

a) MONOCHROMATIC DIFFRACTION LIMITED IMAGE FULL 64^2 ARRAY

b) POLYCHROMATIC IMAGE FULL ARRAY BANDWIDTH FACTOR TWO

c) MONOCHROMATIC IMAGE RANDOM ARRAY 12.5 % OF FULL APERTURE

d) POLYCHROMATIC IMAGE RANDOM ARRAY 12.5 % OF FULL ARRAY BANDWIDTH FACTOR TWO

Figure 24. Polychromatic incoherent imaging, 100% and 12.5% of full array, bandwidth span factor 2.00.

8842–13

a) MONOCHROMATIC IMAGE RANDOM ARRAY 6.25 % OF FULL APERTURE

b) POLYCHROMATIC IMAGE RANDOM ARRAY 6.25% OF FULL APERTURE, BANDWIDTH FACTOR TWO

c) MONOCHROMATIC IMAGE RANDOM ARRAY 3.125 % OF FULL APERTURE

d) POLYCHROMATIC IMAGE RANDOM ARRAY 3.125 % OF FULL APERTURE BANDWIDTH FACTOR TWO

Figure 25. Polychromatic incoherent imaging, 6.25% and 3.125% of full array, bandwidth span factor 2.00.

a) COHERENT 64^2 FULL ARRAY

Figure 26. Partially coherent imaging.

8E42-12 (b)

b) INCOHERENT 64^2 FULL ARRAY

Figure 62. (Continued)

c) PARTIALL COHERENT 64^2
FULL ARRAY

Figure 62. (Continued)

each containing 512 elements. The full array is composed of 4096 elements. The four aperture configurations were generated by using the first four sequences of random numbers produced by the random number generating routine. High signal-to-noise ratios were used in this simulation to isolate the thinning factor effects from the noise effects in degrading image quality. The image quality achievable with random arrays thinned to 12.5% of the full array compares favorably with the quality achievable with the full diffraction-limited array.

One advantage of random arrays is that the image quality does not suffer catastrophic degradation when a large fraction of the array elements fails (see Section 1). The graceful degradation of random array images when large fractions of array elements are removed is shown in Figure 13. Here, the random array elements were removed randomly, with 50% of the elements removed each time. Starting at 1024 elements in a random array thinned to 25% of the full array number, Figure 13(b,c,e,f) represents random arrays thinned to 25%, 12.5%, 6.25%, and 3.125% of the full array. In each case, when random arrays with fewer elements are created, these arrays are subsets of the previous larger arrays. An examination of the random array images in Figure 13 shows that there is no drastic change in image quality until thinning has been reduced to below the 5% level (Figure 13(f)). High S/N conditions also prevailed in this sequence of simulations.

Another advantage of thinned random arrays (one mentioned previously) is that system resolution can be increased dramatically with the same number of array elements in use. All that is necessary is to spread the fixed number of elements over a larger aperture area. This is vividly depicted in Figure 14. A 400-element full array was used as a reference for comparison. The resolution achievable with a full 400-element array, with aperture size of 20 x 20 pixels, is shown in Figure 14(a). Merely redistributing the 400 elements onto larger size aperture limits, as was done in Figure 14(b,c), significantly improved resolution without noticeably degrading image quality. Here, a threefold increase in resolution was achieved (see Figure 14(a and c)). For a comparison of image quality, full array diffraction-limited images corresponding to the increased

aperture sizes are shown in Figure 14(e,f). These two full arrays were comprised of 1936 and 4096 elements, respectively.

Figures 15 and 16 show the effect of low S/N ratio conditions on image quality. A Gaussian noise spectrum was added to each array element to simulate the effect of receiver noise. The variance of the Gaussian spectrum was adjusted relative to the average intensity of the Fourier components to produce the S/N ratios shown. Figures 12(c, d) and 13(c, d) represent the image quality obtained from random arrays with 512 elements (12.5% of the full array) for the S/N ratios shown. The corresponding full array images for identical S/N ratios are shown below each random array image. For S/N ratios above 3, the random array image quality differs little from the full array images.

2. Coherent Imaging

Results of the computer simulation studies of coherent imaging with random and regular arrays are shown in Figures 17 and 18. In this sequence of simulations, the number of overlays is varied to determine the effect of speckle averaging on image quality. In each figure, the random array images are shown on the right side, with the corresponding full array images shown on the left. An aperture size of 64 x 64 pixels is used, and the random array was thinned to 50% of the number of full array elements. A high S/N ratio prevailed in these simulations. For the coherent imaging case, the OTF is the aperture configuration itself. Therefore, when an element of the array is removed, as in a thinned array, the spatial frequency corresponding to that array element is not sampled at all.

Speckle effects severly degrade image quality. For the random array used, speckle effects still are prominent even after 100 overlays, while for the full array, speckles can be significantly removed at 100 overlays. For lower numbers of overlays (e.g., less than 10 in this case), the speckles are quite severe in both situations.

3. Turbulence Effects

The effect of atmospheric turbulence on image quality obtainable from random and regular array incoherent imaging is shown in Figure 19 for which a random array thinned to 12.5% of the full array elements was used. Turbulence levels ranging from moderate to severe were used. The random array images are again shown on the left column and the full array images on the right. The image quality obtained with the 12.5% random arrays is degraded more severely than the corresponding full array images. For moderate turbulence levels ($\sigma \simeq 0.5$), the difference in image quality is slight between the random and full arrays for higher levels of turbulence, but since images are severely degraded anyway, comparisons between them are less meaningful. There seems to be no evidence from this experiment to support the idea that the phase aberration immunity for thinned random arrays, discussed in Section 2.C, is of any value for images of this class.

4. Polychromatic Incoherent Imaging

The results of our computer simulation studies of polychromatic incoherent imaging with random arrays are summarized below. Typical results are shown in Figures 20 through 25. In these studies, the object used was a digitized photograph with 8 bits (24 dB) of dynamic range; it contained a high background intensity level. The image was digitized to a 128 x 128 pixel array. The size of the full aperture for the short wavelength limit of the polychromatic bandwidth was chosen to be 64 x 64 elements, thereby producing 4096 resolution elements in the system FOV at this wavelength. In every polychromatic composite average, the percentage of the number of elements of each monochromatic component is kept fixed rather than the number of elements. The number of elements used in the random array simulation studies ranged from 1024 to 32 elements, corresponding to, in separate studies, from 25% to 3.125% of the number of full array elements for apertures varying from 64^2 to 32^2 in dimension. This range corresponded to a factor of two in wavelength. Each figure (20 through 24) includes the monochromatic diffraction-limited 64^2 full aperture image. This is shown as a reference for comparison.

Figure 20 shows two images found with two different random arrays each thinned to 25% of the 64^2 aperture, giving 1024 elements. These are, of course, monochromatic images and show no appreciable degradation due to thinning.

Figure 21 compares the polychromatic images found by averaging full arrays of 64^2 and 56^2 elements with those from two different 25% thinned arrays of the same dimensions. The effect of combining the two simulated wavelengths is very small, and the effects of thinning are entirely negligible. In Figure 22 similar results are seen for arrays of dimension 64^2, 56^2, and 48^2 each thinned to 25% of 64^2, 56^2, and 48^2, respectively.

In Figure 23 for arrays of dimension 64^2, 56^2, 48^2, 40^2, and 32^2, which represent a span of a factor of two in wavelength or bandwidth, the effects of averaging the more blurry long wavelength image with the sharper short wavelength image are more noticeable. But the effects of thinning the full array are still negligible.

Figure 24 again shows a monochromatic diffraction-limited 64^2 full aperture image as a new reference for comparing this and the next figure, Figure 25. In Figure 24(a), a more continuous polychromatic image is shown; it was generated from 10 different monochromatic full array overlays spanning a bandwidth factor of two in the array sizes of from 64^2 to 32^2. A slight loss of resolution may be noted in comparison to the short wavelength monochromatic image in Figure 24(a). In Figure 24(c), the monochromatic image was produced with a random 12.5% of the short-wavelength (64^2) aperture. Some small degradation in comparison with the full-array image can be noted. The polychromatic image, Figure 24(d), although showing less resolution than Figure 24(c), does not show, for example, the ghosting evident in the background.

A similar comparison is made in Figure 25(a and b) for thinning to 6.25%. The degraded short wavelength (64^2) monochromatic image of Figure 25(a) is compared to the polychromatic version of bandwidth factor two in Figure 25(b). The severly degraded 3.125% short wavelength (64^2) monchromatic image of Figure 25(c) is very much improved in the polychromatic factor two bandwidth version in Figure 25(d).

5. Partially Coherent Imaging

The effects of partial coherence on image formation were studied by employing separable monochromatic partial coherence functions of the kind illustrated in Figure 2. In one set of experiments, speckle formation was studied as a function of the degree of coherence. As was expected, the variance of the speckle distribution function decreased as the coherence was reduced. The dramatic difference between coherent and incoherent imaging may be seen by comparing Figure 25(a) with Figure 26(b), respectively. The coherent picture, without any added random phase, displays the vivid edge "ringing" expected from the diffraction of sharp boundaries. This can be noted in the border of the picture in the face of the subject, and along the right side of the subject's hair. The incoherent image, Figure 26(b), shows no obvious comparable effects. The partially coherent image, Figure 26(c), using the 121-term separable coherent function plotted in Figure 2, shows an intermediate degree of diffraction effects. These effects properly are somewhat exaggerated when discrete as opposed to continuous arrays are employed (as noted in Appendix B).

SECTION 3

SUMMARY OF RESULTS

The results from the computer simulation studies of random array imaging suggest that random arrays are primarily useful for incoherent imaging applications. The advantages of random array imaging for incoherent imaging are

Large degree of thinning possible. In this study, we have shown that random arrays thinned to less than 6% of the number of full array elements (4096) produce incoherent image quality comparable to the full array diffraction-limited image quality. The degree of thinning allowable is, in principle, inversely proportional to the square root of the number of elements in the full array, which number is equivalant to the number of elements resolved by the full array in its field of view.

Polychromatic radiation. Thinning to 3% was shown to be similarly effective in the case of broadband with polychromatic imaging.

Easy to design. Many random array configurations produce image qualities comparable to full array diffraction-limited quality. The probability of success can be estimated for choosing an array.

Graceful degradation. The image quality obtainable from random arrays does not suffer catastrophic degradation when large fractions of array elements are removed. The image quality degrades very gracefully.

Increased resolution with fixed number of array elements. The resolving capability of random arrays can be increased significantly using the same number of array elements. This is accomplished by merely redistributing the array elements over a larger aperture size.

Partially coherent imaging proved extraordinarily expensive to simulate, but a separable version of the coherence function was modeled that allowed a cursory examination of the problem. As expected, the behavior of partially coherent images was qualitatively between the coherent and incoherent extremes.

For incoherent imaging in turbulent conditions in the atmosphere, thinned random arrays suffer only slightly in image quality when compared to full array images for a large range of turbulence levels. For lower turbulence levels, the difference in image quality is slight, although the random array images were more degraded. For higher turbulence levels, both arrays suffered severe degradations, and the comparison of image quality under those circumstances is less meaningful.

For coherent imaging applications, random arrays do not offer significant advantages over full arrays. This is because speckle effects cannot be reduced enough by speckle averaging (or overlays), and substantial degradation of image quality still remains after numerous overlays.

APPENDIX A

RANDOM ARRAY DESIGN THEORY

There is a body of microwave antenna literature dating from the 1960s describing the theoretical expectations of large antenna arrays with randomly spaced elements. The tradeoffs between resolution, gain, and sidelobe level have been analyzed in probabilistic terms. These ideas have been experimentally tested, and the results were favorable. Comparisons were also made between relative efficacy of antennas designed algorithmically and those designed by random placement of the elements; the latter showed remarkable advantages. This appendix briefly summarizes some important points from the work of Lo.[1]

The sidelobe level is related to the number of elements and only slightly to the aperture dimension. High resolution can be obtained with few elements, and, for a given number of elements, high resolution can be obtained by spreading these elements without a substantial change in the sidelobe level or the directive gain.

The probability of a sidelobe level below r is $\left[1 - \exp(-Nr^2)\right]^{4a}$, where N is the total number of elements, a is the aperture dimension measured in wavelengths, and r is the sidelobe level with the mainbeam normalized. Figure A-1 is a universal plot of this relationship plotting probability versus $r\sqrt{N}$ for a variety of aperture dimensions indexed by $q = \log_{10} a$. For planar arrays, q is equal to the sum of q_1 and q_2. This family tells the probability of finding ("designing") a random array with a specified maximum sidelobe level for a given aperture and number of elements. Figure A-2 demonstrates the nearly perfect agreement between the probabilistic theory and a computer simulation with randomly positioned antenna arrays.

---

[1] Y.T. Lo and R.J. Simcoe, IEEE Trans. Ant. and Prop., Vol. Ap-15, No. 2, March 1967, pp. 231-235.

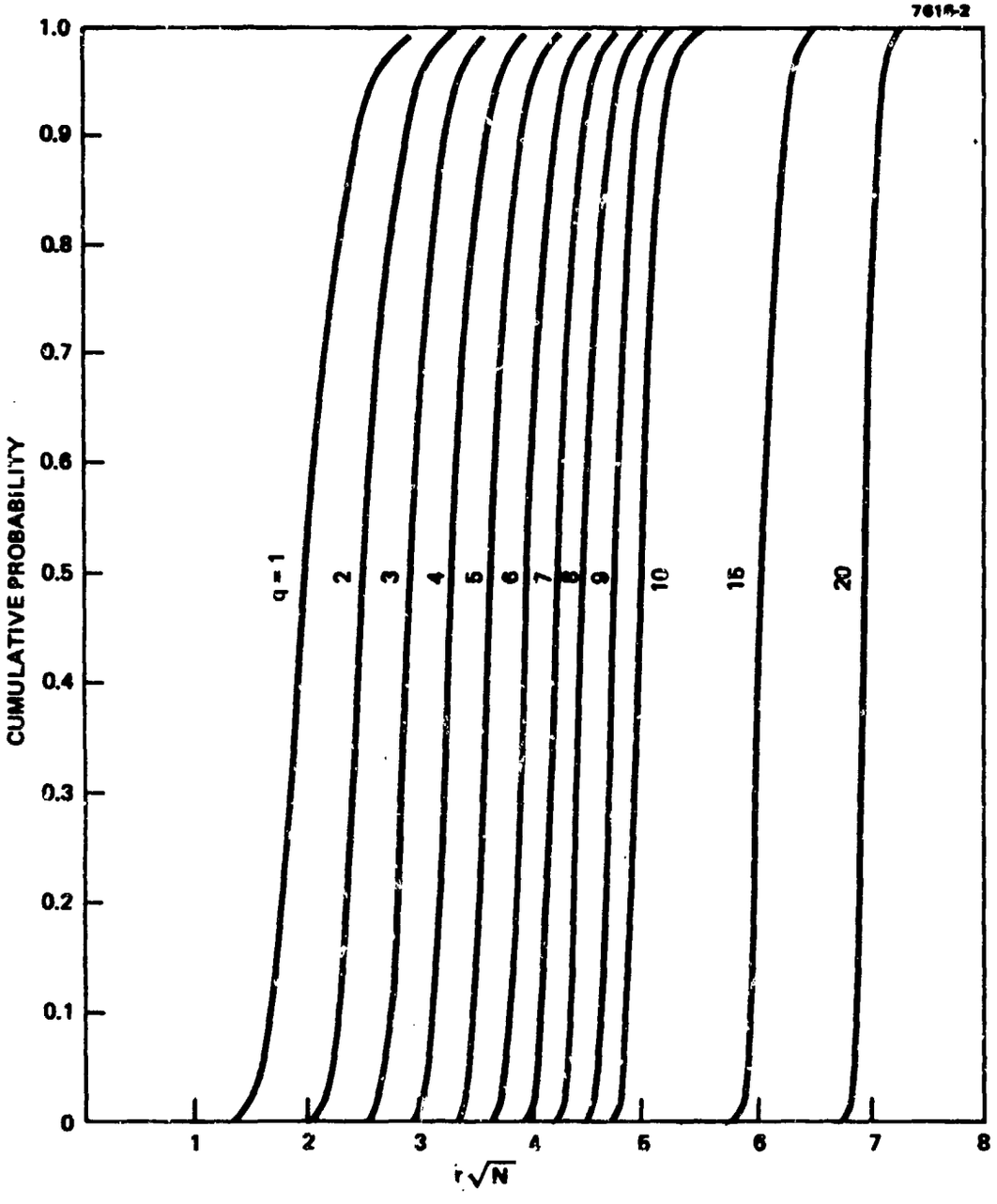

Figure A-1. Theoretical distribution curves for $r\sqrt{N}$, where N = total number of elements, and r = sidelobe level. In the case of a linear array, q = $\log_{10}$ (array length in wavelengths); in the case of a planar array, q = $\log_{10}$ (aperture area in wavelengths squared).

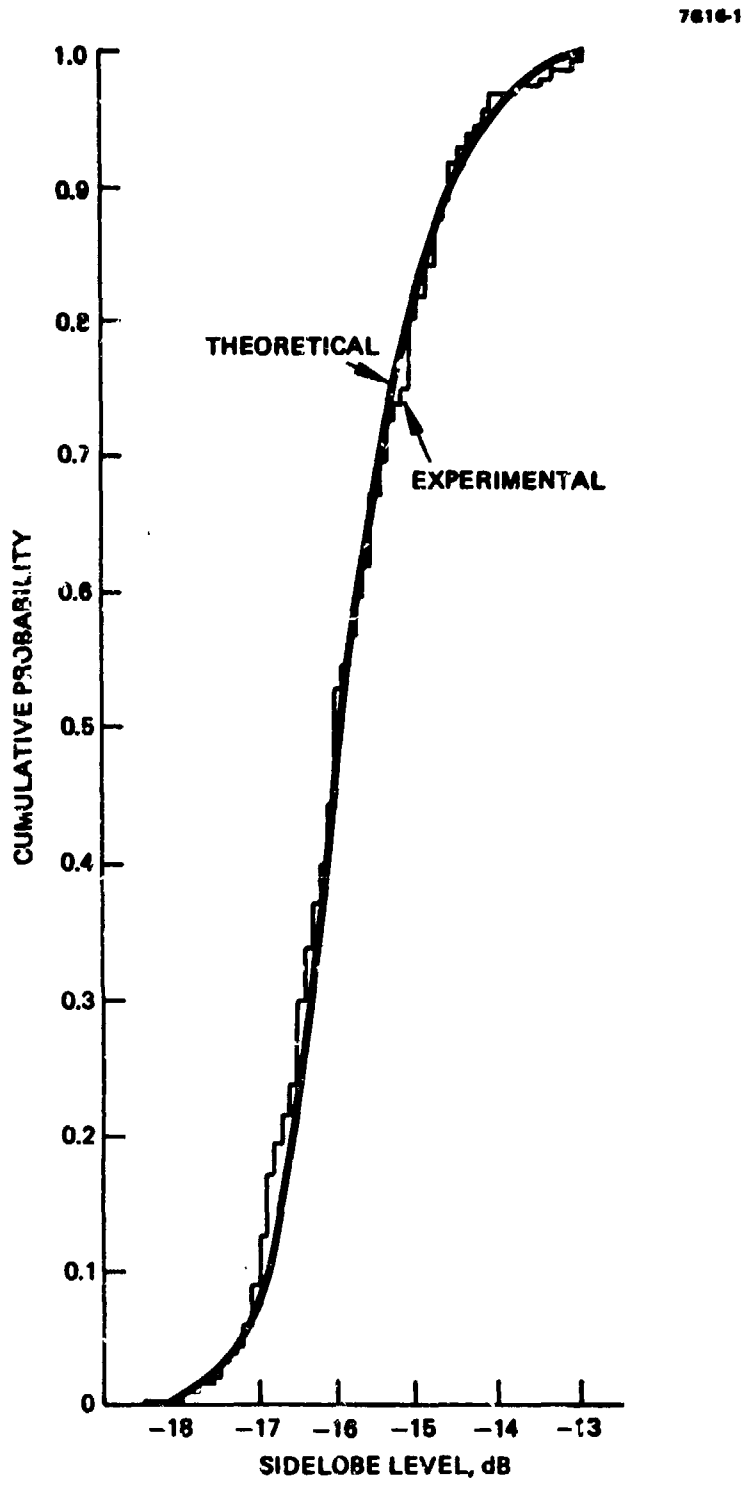

Figure A-2.
Comparison of the theoretical and experimental distributions for the sidelobe levels of linear arrays. The experimental distribution is obtained from 180 pseudo-random linear arrays generated by two planar arrays.

APPENDIX B

DIFFRACTION EFFECTS IN DISCRETE COHERENT IMAGES

The general effects of diffraction in coherent images are well known but there are novel striking effects when the arrays are discrete rather than continuous. Especially strong symmetric effects can be seen when the imaging array is full and the number of elements in the array and in the object is commensurate. In Figure B-1, the coherent images of a 64^2 bright uniform object produced by four different full arrays are shown. In Figure B-1(a), a 64^2 full aperture was used, and 16^2 bright crossed lines appear in the image. In Figures B-1(b), B-1(c), and B-1(d), 7^2, 8^2, and 9^2 full apertures were employed, respectively. The four bright corners in the images are much more distinct in the case of the 8^2 aperture, which is, of course, commensurate with 64^2. The diffraction effects of the 64^2 aperture can be noted in the coherent and partially coherent images in Figure 26.

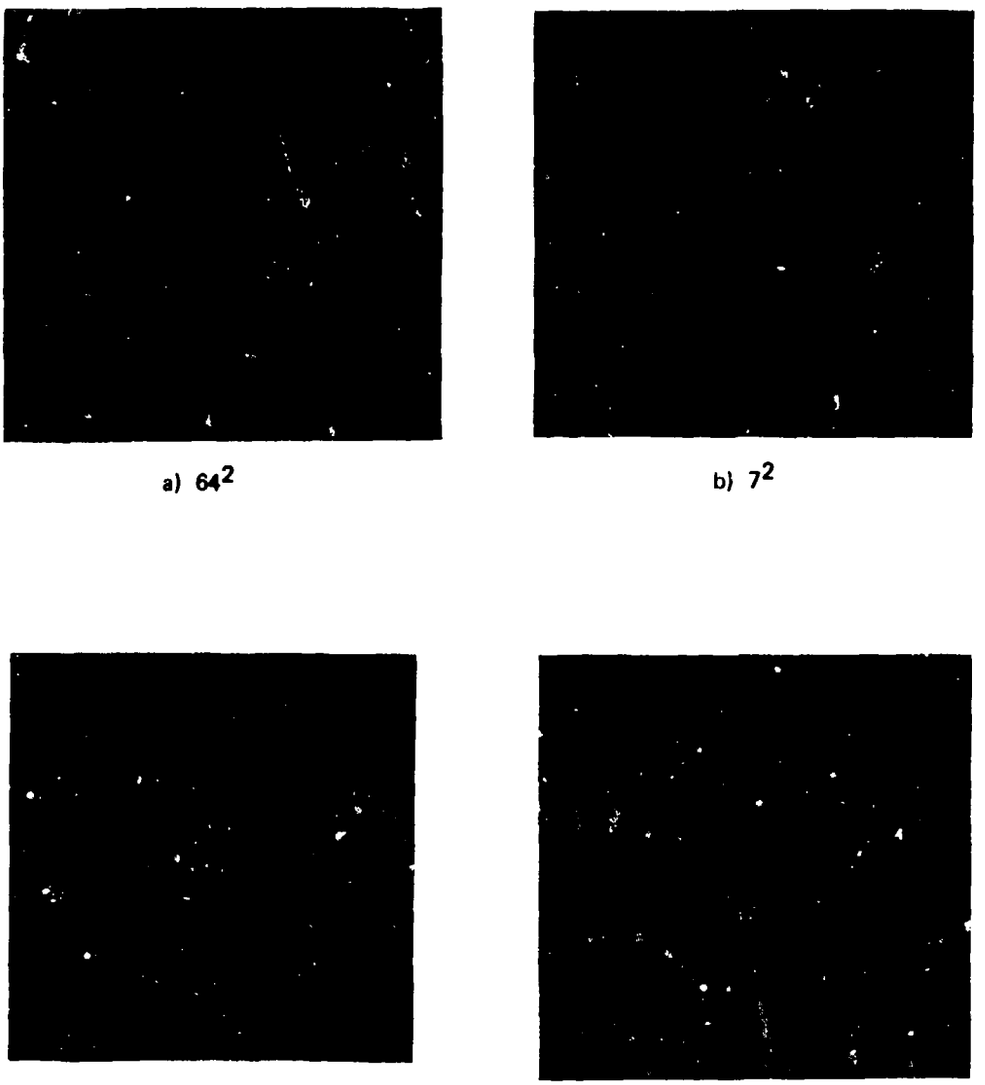

a) 64^2 b) 7^2

c) 8^2 d) 9^2

Figure B-1. Diffraction effects in coherent imaging with discrete arrays. Images at a 64^2 uniform object with full apertures of sizes: a) 64^2, b) 7^2, c) 8^2, d) 9^2.

APPENDIX C

SEPARABLE REPRESENTATION OF THE DEGREE OF COHERENCE FUNCTION

Let (X,Y) be the pixel location of the vector $\bar{u}$ in Eq. 22.

$A_o = 126 \times 2^{-9}$ $A_2 = 120 \times 2^{-9}$ $A_4 = 10 \times 2^{-9}$

$A_1 = 210 \times 2^{-9}$ $A_3 = 45 \times 2^{-9}$ $A_5 = 2^{-9}$ in Eq. 21.

$\alpha = 2^{-6}$

The M = 121 terms for each f_n in Eq. 22 are:

(1)	A_o		(18)	$\sin(2Y) \cdot \sqrt{2A_oA_2}$	
(2)	$\cos(X) \cdot \sqrt{2A_oA_1}$		(19)	$\sin(3Y) \cdot \sqrt{2A_oA_3}$	
(3)	$\cos(2X) \cdot \sqrt{2A_oA_2}$		(20)	$\sin(4Y) \cdot \sqrt{2A_oA_4}$	
(4)	$\cos(3X) \cdot \sqrt{2A_oA_3}$		(21)	$\sin(5Y) \cdot \sqrt{2A_oA_5}$	
(5)	$\cos(4X) \cdot \sqrt{2A_oA_4}$		(22)	$\cos(X-Y) \cdot \sqrt{A_1^2}$	
(6)	$\cos(5X) \cdot \sqrt{2A_oA_5}$		(23)	$\cos(X-2Y) \cdot \sqrt{A_1A_2}$	
(7)	$\sin(X) \cdot \sqrt{2A_oA_1}$		(24)	$\cos(X-3Y) \cdot \sqrt{A_1A_3}$	
(8)	$\sin(2X) \cdot \sqrt{2A_oA_2}$		(25)	$\cos(X-4Y) \cdot \sqrt{A_1A_4}$	
(9)	$\sin(3X) \cdot \sqrt{2A_oA_3}$		(26)	$\cos(X-5Y) \cdot \sqrt{A_1A_5}$	
(10)	$\sin(4X) \cdot \sqrt{2A_oA_4}$		(27)	$\cos(2X-Y) \cdot \sqrt{A_2A_1}$	
(11)	$\sin(5X) \cdot \sqrt{2A_oA_5}$		(28)	$\cos(2X-2Y) \cdot \sqrt{A_2^2}$	
(12)	$\cos(Y) \cdot \sqrt{2A_oA_1}$		(29)	$\cos(2X-3Y) \cdot \sqrt{A_2A_3}$	
(13)	$\cos(2Y) \cdot \sqrt{2A_oA_2}$		(30)	$\cos(2X-4Y) \cdot \sqrt{A_2A_4}$	
(14)	$\cos(3Y) \cdot \sqrt{2A_oA_3}$		(31)	$\cos(2X-5Y) \cdot \sqrt{A_2A_5}$	
(15)	$\cos(4Y) \cdot \sqrt{2A_oA_4}$		(32)	$\cos(3X-Y) \cdot \sqrt{A_3A_1}$	
(16)	$\cos(5Y) \cdot \sqrt{2A_oA_5}$		(33)	$\cos(3X-2Y) \cdot \sqrt{A_3A_2}$	
(17)	$\sin(Y) \cdot \sqrt{2A_oA_1}$		(34)	$\cos(3X-3Y) \cdot \sqrt{A_3^2}$	

(35) $\cos(3X-4Y) \cdot \sqrt{A_3A_4}$

(36) $\cos(3X-5Y) \cdot \sqrt{A_3A_5}$

(37) $\cos(4X-Y) \cdot \sqrt{A_4A_1}$

(38) $\cos(4X-2Y) \cdot \sqrt{A_4A_2}$

(39) $\cos(4X-3Y) \cdot \sqrt{A_4A_3}$

(40) $\cos(4X-4Y) \cdot \sqrt{A_4A_4}$

(41) $\cos(4X-5Y) \cdot \sqrt{A_4A_5}$

(42) $\cos(5X-Y) \cdot \sqrt{A_5A_1}$

(43) $\cos(5X-2Y) \cdot \sqrt{A_5A_2}$

(44) $\cos(5X-3Y) \cdot \sqrt{A_5A_3}$

(45) $\cos(5X-4Y) \cdot \sqrt{A_5A_4}$

(46) $\cos(5X-5Y) \cdot \sqrt{A_5A_5}$

(47) $\sin(X-Y) \cdot \sqrt{A_1^2}$

(48) $\sin(X-2Y) \cdot \sqrt{A_1A_2}$

(49) $\sin(X-3Y) \cdot \sqrt{A_1A_3}$

(50) $\sin(X-4Y) \cdot \sqrt{A_1A_4}$

(51) $\sin(X-5Y) \cdot \sqrt{A_1A_5}$

(52) $\sin(2X-Y) \cdot \sqrt{A_2A_1}$

(53) $\sin(2X-2Y) \cdot \sqrt{A_2A_2}$

(54) $\sin(2X-3Y) \cdot \sqrt{A_2A_3}$

(55) $\sin(2X-4Y) \cdot \sqrt{A_2A_4}$

(56) $\sin(2X-5Y) \cdot \sqrt{A_2A_5}$

(57) $\sin(3X-Y) \cdot \sqrt{A_3A_1}$

(58) $\sin(3X-2Y) \cdot \sqrt{A_3A_2}$

(59) $\sin(3X-3Y) \cdot \sqrt{A_3A_3}$

(60) $\sin(3X-4Y) \cdot \sqrt{A_3A_4}$

(61) $\sin(3X-5Y) \cdot \sqrt{A_3A_5}$

(62) $\sin(4X-Y) \cdot \sqrt{A_4A_1}$

(63) $\sin(4X-2Y) \cdot \sqrt{A_4A_2}$

(64) $\sin(4X-3Y) \cdot \sqrt{A_4A_3}$

(65) $\sin(4X-4Y) \cdot \sqrt{A_4A_4}$

(66) $\sin(4X-5Y) \cdot \sqrt{A_4A_5}$

(67) $\sin(5X-Y) \cdot \sqrt{A_5A_1}$

(68) $\sin(5X-2Y) \cdot \sqrt{A_5A_2}$

(69) $\sin(5X-3Y) \cdot \sqrt{A_5A_3}$

(70) $\sin(5X-4Y) \cdot \sqrt{A_5A_4}$

(71) $\sin(5X-5Y) \cdot \sqrt{A_5A_5}$

(72) $\cos(X+Y) \cdot \sqrt{A_1A_1}$

(73) $\cos(X+2Y) \cdot \sqrt{A_1A_2}$

(74) $\cos(X+3Y) \cdot \sqrt{A_1A_3}$

(75) $\cos(X+4Y) \cdot \sqrt{A_1A_4}$

(76) $\cos(X+5Y) \cdot \sqrt{A_1A_5}$

(77) $\cos(2X+Y) \cdot \sqrt{A_2A_1}$

(78) $\cos(2Y+2Y) \cdot \sqrt{A_2A_2}$

(79) $\cos(2X+3Y) \cdot \sqrt{A_2A_3}$

(80) $\cos(2X+4Y) \cdot \sqrt{A_2A_4}$

(81) $\cos(2X+5Y) \cdot \sqrt{A_2A_5}$

(82) $\cos(3X+Y) \cdot \sqrt{A_3A_1}$

(83) $\cos(3X+2Y) \cdot \sqrt{A_3A_2}$

(84) $\cos(3X+3Y) \cdot \sqrt{A_3A_3}$

(85) $\cos(3X+4Y) \cdot \sqrt{A_3A_4}$

(86) $\cos(3X+5Y) \cdot \sqrt{A_3A_5}$

(87) $\cos(4X+Y) \cdot \sqrt{A_4A_1}$

(88) $\cos(4X+2Y) \cdot \sqrt{A_4A_2}$

(89) $\cos(4X+3Y) \cdot \sqrt{A_4A_3}$

(90) $\cos(4X+4Y) \cdot \sqrt{A_4A_4}$

(91) $\cos(4X+5Y) \cdot \sqrt{A_4A_5}$

(92) $\cos(5X+Y) \cdot \sqrt{A_5A_1}$

(93) $\cos(5X+2Y) \cdot \sqrt{A_5A_2}$

(94) $\cos(5X+3Y) \cdot \sqrt{A_5A_3}$

(95) $\cos(5X+4Y) \cdot \sqrt{A_5A_4}$

(96) $\cos(5X+5Y) \cdot \sqrt{A_5A_5}$

(97) $\sin(X+Y) \cdot \sqrt{A_1A_1}$

(98) $\sin(X+2Y) \cdot \sqrt{A_1A_2}$

(99) $\sin(X+3Y) \cdot \sqrt{A_1A_3}$

(100) $\sin(X+4Y) \cdot \sqrt{A_1A_4}$

(101) $\sin(X+5Y) \cdot \sqrt{A_1A_5}$

(102) $\sin(2X+Y) \cdot \sqrt{A_2A_1}$

(103) $\sin(2X+2Y) \cdot \sqrt{A_2A_2}$

(104) $\sin(2X+3Y) \cdot \sqrt{A_2A_3}$

(105) $\sin(2X+4Y) \cdot \sqrt{A_2A_4}$

(106) $\sin(2X+5Y) \cdot \sqrt{A_2A_5}$

(107) $\sin(3X+Y) \cdot \sqrt{A_3A_1}$

(108) $\sin(3X+2Y) \cdot \sqrt{A_3A_2}$

(109) $\sin(3X+3Y) \cdot \sqrt{A_3A_3}$

(110) $\sin(3X+4Y) \cdot \sqrt{A_3A_4}$

(111) $\sin(3X+5Y) \cdot \sqrt{A_3A_5}$

(112) $\sin(4X+Y) \cdot \sqrt{A_4A_1}$

(113) $\sin(4X+2Y) \cdot \sqrt{A_4A_2}$

(114) $\sin(4X+3Y) \cdot \sqrt{A_4A_3}$

(115) $\sin(4X+4Y) \cdot \sqrt{A_4A_4}$

(116) $\sin(4X+5Y) \cdot \sqrt{A_4A_5}$

(117) $\sin(5X+Y) \cdot \sqrt{A_5A_1}$

(118) $\sin(5X+2Y) \cdot \sqrt{A_5A_2}$

(119) $\sin(5X+3Y) \cdot \sqrt{A_5A_3}$

(120) $\sin(5X+4Y) \cdot \sqrt{A_5A_4}$

(121) $\sin(5X+5Y) \cdot \sqrt{A_5A_5}$

APPENDIX D

BIBLIOGRAPHY

Y. T. Lo, "A Mathematical Theory of Antenna Arrays with Randomly Spaced Elements" IRE Trans. Antennas Propagat. AP-12 pp. 257-268, May 1964.

Y. T. Lo, "A Probabilistic Approach to the Problem of Large Antenna Arrays," Radio Sci. 68D, pp. 1011-1019, Sept. 1964.

T. T. Lo and R. J. Simcoe, "An Experiment on Antenna Arrays with Randomly Spaced Elements," IEEE Trans. Antennas Propagat. AP-15, pp. 231-235, Mar. 1967.

A. R. Panicali and Y. T. Lo, "A Probabilistic Approach to Large Circular and Spherical Arrays," IEEE Trans. Antennas Propagat. AP-17, pp. 514-522, July 1969.

V. D. Agrawal and Y. T. Lo, "Distribution of Sidelobe Level in Random Arrays," Proc IEEE (Lett.) 57, pp. 1764-1765, Oct. 1969.

J. W. Goodman, Introduction to Fourier Optics (McGraw Hill, 1968).

B. D. Steinberg, "The Peak Sidelobe of the Phased Array Having Randomly Located Elements," IEEE Trans. Antenna Propagat. AP-20, pp. 129-136, March 1972.

B. D. Steinberg, "Comparison between the Peak Sidelobe of Random Array and Algorithmically Disposed Aperiodic Arrays," IEEE Trans. Antenna Propagat. AP-21, pp. 336-370, May 1973.

B. D. Steinberg, Principles of Aperture and Array System Design. N.Y.: Wiley, 1976.

M. B. Donvito and S. A. Kassam, "Characterization of the Random Array Peak Sidelobe," IEEE Trans. Antenna Propagat. AP-27, pp. 379-389, May 1979.

W. T. Cathey, "Optical Information Processing and Holography," Wiley, 1974.

APPENDIX E

PERSONNEL AND PAPERS

The following people contributed to the technical performance of this contract: David Y. Tseng, Bernard H. Soffer, Richard Frey, Gary Edwards, and Sheldon Katz. One manuscript, entitled "Imaging with Random Arrays," is in preparation for submission to Applied Optics.